Politecnico di Torino

Master of Science in Energy and Nuclear Engineering

Academic Year 2020-2021

October 2021

Impact of runaway electrons generated during disruptions on the first wall of the tokamak reactors

Supervisors:

Prof. Fabio Subba (PoliTo)

Prof. Roberto Bonifetto (PoliTo)

Prof. Matteo Passoni (PoliMi)

Student:

Lovepreet Singh

Summary

Nuclear fusion is considered a promising alternative for power generation, potentially superior to fission, due to reduced operation radioactivity, the low nuclear waste production, and the intrinsic impossibility to develop a diverging reaction. Extensive research in the development of this power source is ongoing for several decades now. The next generation of Tokamak devices (the ITER reactor under construction and, later, DEMO), is the first expected to produce more power than that needed to sustain the nuclear reactions.

One of the possible show-stoppers in the operation of the tokamak fusion reactors is the occurrence of disruptions, un-controlled events leading potentially to the deposition of a few GJ energy onto the wall in a few ms. On a DEMO-size machine, a disruption could potentially damage the wall un-recoverably. From a theoretical point of view, disruptions can be caused by a variety of events including MHD instabilities, malfunctioning of control systems, etc.

A considerable fraction of the energy dissipated during a disruption can be carried by runaway electrons, a beam of electrons accelerated to relativistic energies by the intense electric field developing during such an event. Their generation and evolution are not yet fully understood by the fusion community, which further complicates the problem of the selection of structural materials and the design of the cooling system able to handle the high heat loads involved in the disruptions and the impact of Runaway Electrons (REs). The Dreicer mechanism is the primary generation mechanism for the current reactors, while in the future reactors the avalanche mechanism is expected to take this role. The mitigation systems are the Massive Gas Injection (MGI), Shattered Pellet Injection (SPI), Resonant Magnetic Perturbation (RMP), and Magnetic Energy Transfer (MET). However, the MGI and SPI can lead to an additional generation of runaways, so further investigations are required for all these mitigation systems.

The thesis analyzes the impact of runaway electrons generated during disruptions in different cases,using the Monte Carlo based code FLUKA. Firstly, the runaway current damage to the first wall of existing tokamak reactors is presented, along with its generation mechanisms and mitigation systems. Then, we reproduce and complete a case-study firstly drafted by ENEA. This consis of bombarding a sample geometry, built taking as reference the EU-DEMO First Wall, with REs having an energy of 20 MeV. It was seen that, depending on the angle of impact considered, a different amount of energy is deposited in the structure. As also, different deposition curves are obtained according to the structural materials considered.

In the future, we plan to extend this work to reproduce, to a certain extent, the measurements given by the diagnostics in the JET fusion device, providing measurements on the Soft and Hard X-rays. These X-rays are the secondary

particles generated by the REs impacting onto the wall, and could be traced by the virtual detectors embedded in FLUKA. Therefore, this would show the capabilities of FLUKA in reproducing the real measurements, helping to clear the picture of how REs interacts with the different structural materials present in the main chamber of JET. Afterward, the study could be scaled up to EU-DEMO where Tungsten will be the main plasma-facing component to handle the REs.

Acknowledgments

I will always be grateful to my main supervisor Prof. Fabio Subba for his support, kindness, and innumerable ways in which he had guided me in my career. I thank him for all that he has done, for being an amazing supervisor, professor, and mentor, and for guiding me on the right path.

I would like to express my sincere gratitude to Prof. Roberto Bonifetto who in spite of his very busy schedule and commitments, always made himself available to help me throughout my MSc studies.

A heartfelt acknowledgment to Ing. Giuseppe Francesco Nallo and Prof. Matteo Passoni for taking part in this important chapter of my life. In particular, I would like to thank Ing. Nallo for enriching my studies with his experience and curiosity and Prof. Passoni for accepting to be my thesis supervisor.

I gratefully recognize the help of Dr. Francesco Maviglia and Dr. Gabriella Pautasso for inspiring me in this new endeavor. This work would stay incomplete without the support of Dr. Pautasso who selflessly took this project to heart and without her the access to JET data would remain impossible.

My appreciation also goes out to my family and friends for their encouragement and support all through my studies. In particular, I would like to thank my friend Chiara for helping me to solve any technical issue with the software and my colleague Massimo for carrying out all the MSc projects with me. Last but not least, I thank my sister Kamal for annoying me throughout the semesters passed at home during multiple lockdowns.

Contents

List of figures

1. Introduction

Nuclear fusion is considered a promising alternative for power generation, potentially superior to fission, due to reduced operation radioactivity, low nuclear waste production, and the intrinsic impossibility to develop a diverging reaction. Extensive research in the development of this power source is ongoing for several decades now. The next generation of Tokamak devices that are the International Thermonuclear Experiment Reactor (ITER) and, later, the DEMOnstration Power Plant (DEMO), is the first expected to produce more power than that needed to sustain the nuclear reactions (Nordlund, 2018).

One of the many open issues that the community is trying to tackle is related to the disruptions. They are un-controlled events leading potentially to the deposition of a few GJ energy onto the wall of large machines in a few ms. Disruption simulations in large tokamaks such as ITER have shown that future machines like ITER and DEMO, which will store more internal energy with respect to present devices, are prone to cause severe damages (Rosenbluth, 1997). In figure 1, the sizes of the different reactors are shown. It can be noticed that the corresponding powers involved are increasing at a faster pace. As a consequence, on a DEMO-size machine, a disruption could potentially damage the wall un-recoverably.

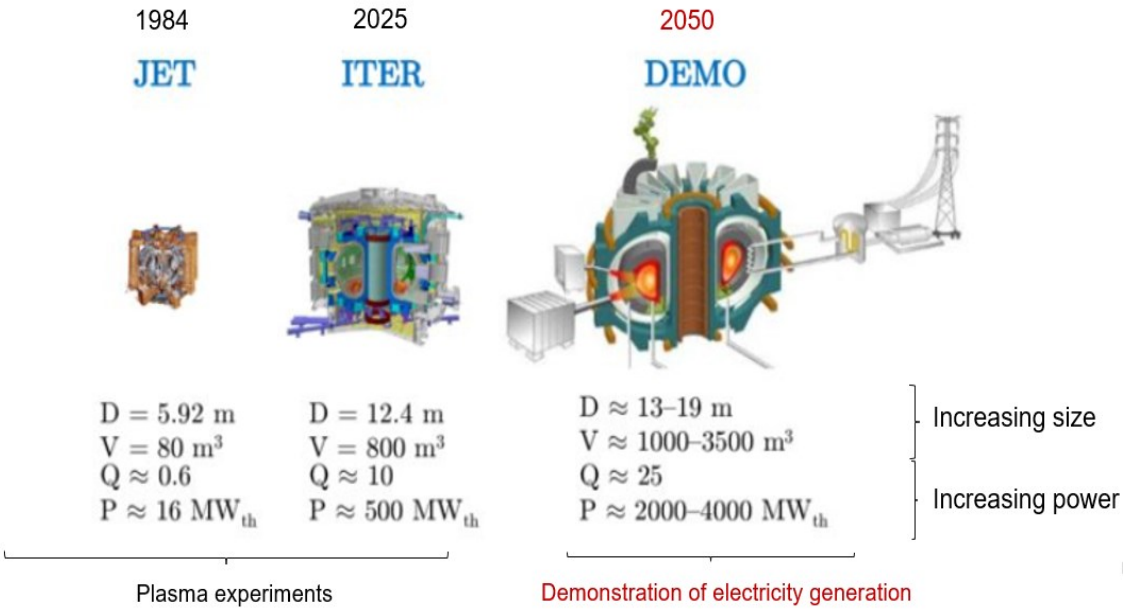

Figure 1 Dimensions and Powers of the different fusion reactors (Dubus, 2014)

Furthermore, while present devices are being used to implement plasma experiments in order to study the plasma physics or the different components of

a fusion reactor, DEMO will have the task to demonstrate the electricity generation from fusion, which poses several additional challenges. As a consequence, to produce electricity at a competitive price, it is needed that events like disruptions do not occur during the operation of DEMO or a future industrial plant. Indeed, these events would result, at least, in the replacement of some components of the machine; such an operation would be both costly and time-consuming.

The fusion community is highly sensitive to the threat represented by the disruptions and, for this reason, these events are addressed several times in the EUROfusion roadmap to the realization of fusion energy (Nordlund, 2018). In particular, by 2030 ITER will have to demonstrate the optimal plasma conditions that would minimize the occurrence of the disruptions along with validating the disruption mitigation systems.

Disruptions damage the tokamak structure through three ways: (1) electromagnetic forces; (2) thermal loads; (3) Runaway Electrons (REs) (Plyusnin et al., 2012). Electromagnetic forces cause the plasma displacement that can result in plasma hitting the first wall (FW) of the machine, the thermal loads lead to huge energies discharged on the Plasma Facing Components (PFCs) that can melt and damage them permanently and the REs, which are generated during the current quench phase of a disruption, lead to local damage on the FW by different means.

The thesis focuses on runaway electrons. The REs are a beam of electrons accelerated to relativistic energies by the intense electric field developing during a disruption. They can carry a current up to 60-70% of the pre-disruptive plasma current (Plyusnin et al., n.d.). The reasons for studying these electron beams are multiple: (1) although they do not always represent a severe problem for the current reactors, in future tokamaks they can cause permanent damages to the PFCs; (2) the study of their generation mechanism is fundamental for the design of disruption mitigation systems that do not cause additional REs generation; (3) their impact on PFCs leads to the activation of the materials which complicate the maintenance operations.

Since their presence represents a problem for the fusion machines, multiple systems are under study to suppress their generation during a disruption or mitigate their effects. These are the Massive Gas Injection (MGI), Shattered Pellet Injection (SPI), Resonant Magnetic Perturbation (RMP), and Magnetic Energy Transfer (MET). However, each of these systems has some issues that are still to be addressed and strengthen the motivation to study the generation process of REs in Tokamaks.

Along with describing the theoretical aspects related to the REs, an analysis has been carried out considering the impact of these electrons on the first wall (FW) of DEMO with different incidence angles. The activity has been done using the

Monte Carlo-based code FLUKA and the results have been compared with a study done by ENEA. In addition, the REs energy distributions observed in JET through HXR diagnostics are reproduced using FLUKA.

Firstly, an introduction about the basic notions needed to understand the physics of REs is presented in section 2. After that, the reasons for which the REs are a serious threat for future fusion machines are thoroughly described in section 3, which also shows a few examples of the damage caused by them in some of the existing tokamaks, section 4 presents the processes that lead to the generation of relativistic electrons during the occurrence of disruptions, with a description of the two main generation mechanisms. In section 5 the above-mentioned mitigation and suppression mechanisms are described together with the open issues of these systems. In section 6 the FLUKA code is briefly described with its features necessary for this study and section 7 describes the activity carried out in the framework of the thesis, with a brief description of the EU-DEMO FW structure, and the presentation of the results. Section 8 discusses the reproduction of some of the REs energy distribution observed in JET. Finally, in the last section, our conclusions and perspectives are given.

2. Introduction to the tokamak reactor

In order to allow the fusion reactions to take place and have power production, the plasma has to be confined for a sufficiently long time. In tokamaks, this confinement is obtained through the application of magnetic fields produced by multiple coils present around the central region of a tokamak and a central solenoid present at the center of the machine. That is a tokamak reactor is a magnetic confinement device designed to produce power through fusion reactions that take place inside the plasma. In figure 2 a schematic representation of a tokamak reactor is given.

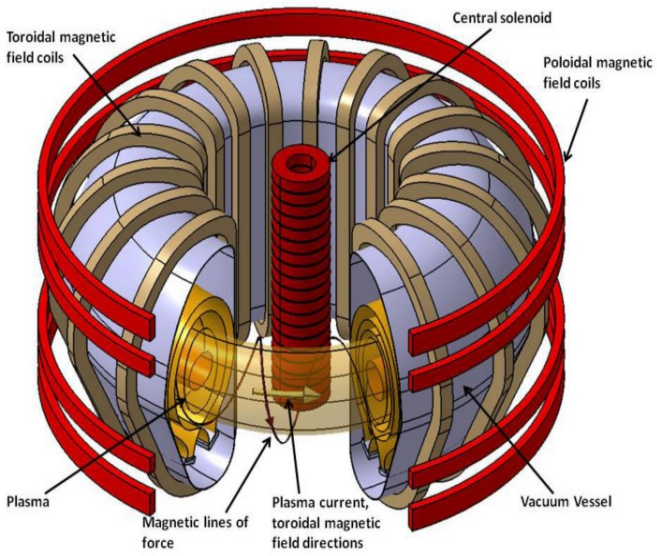

Figure 2 Schematic representation of a tokamak reactor (Cizek et al., 2019)

The magnetic field responsible for the confinement is made of different components. The toroidal magnetic field coils generate the toroidal magnetic field while the poloidal magnetic field is produced through the plasma current induced by the central solenoid and the poloidal magnetic field coils. The plasma current is generated inducing a current in the central solenoid. This pulsed current generates a time-varying magnetic field which in turn generate an electric field as explained by Faraday's law (1),

$$\Delta \times E = -\frac{\partial B}{\partial t} \quad (1)$$

The electric field generates the plasma current as described by ohm's law,

$$E = rJ \quad (2)$$

The current density (J) integrated over the whole plasma cross section gives the plasma current flowing in the toroidal direction, that is the direction identified

by the toroidal magnetic field in figure 2. The parameter r in expression (2) is the plasma resistivity which is proportional to $T_e^{-3/2}$. Since the plasma temperature represented by the electron temperature (T_e) is around 10 keV, during normal operation, the plasma resistivity is extremely low making the plasma superconductive. Moreover, the change in the pulsed magnetic field which passes through the central solenoid generates a loop voltage around the torus, and this voltage increases with the induced field (De Vries, 2019).

The poloidal and toroidal magnetic fields generate the final magnetic field of helical shape able to confine the plasma in the central region. The toroidal field, the plasma current with the resulting magnetic lines are shown in figure 2.

For a better representation of the different field components in figure 3 a representation of plasma with toroidal magnetic fluxes defined by a constant poloidal magnetic flux is shown.

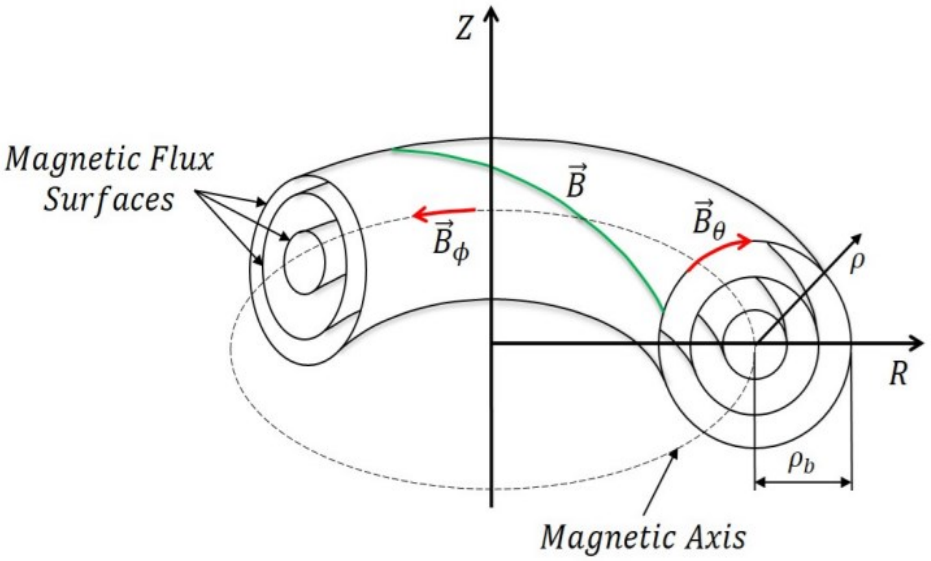

Figure 3 Schematic of plasma with the toroidal magnetic flux surfaces. ϕ, θ and R define the toroidal, poloidal, and radial direction, respectively (Barton et al., 2015)

In figure 3, the magnetic field $\vec{B}$ (green line) is given by the combination of the toroidal magnetic field (B_ϕ) and the poloidal magnetic field (B_θ). Moreover, Z defines the vertical direction and R the radial direction whereas ρ is the plasma minor radius and ρ_b is the minor radius of the last closed magnetic flux surface (Barton et al., 2015). Along with the vertical and the radial direction, there are other two important directions in a tokamak that are the toroidal direction identified by the toroidal magnetic field and the poloidal direction identified by the poloidal magnetic field. Moreover, most of the plasma parameters like temperature, electron density are usually shown along the radial direction to

observe the differences between the central region of a plasma, around the inner first wall which protects the central solenoid, and the external region, near the external first wall.

Apart from the coils needed to generate the magnetic field necessary to confine the plasma, a tokamak can include also some other coils which may have different features. For instance, the RMP system uses external coils to mitigate the runaway electrons by generating magnetic perturbation. In particular, in TEXTOR a dynamic ergodic divertor (DED) is used to generate perturbations in the plasma. In figure 4, the DED is shown, and can be noticed that they are placed at the high field side of the torus in order to reach the plasma core where most of the REs are generated (Finken et al., 2004).

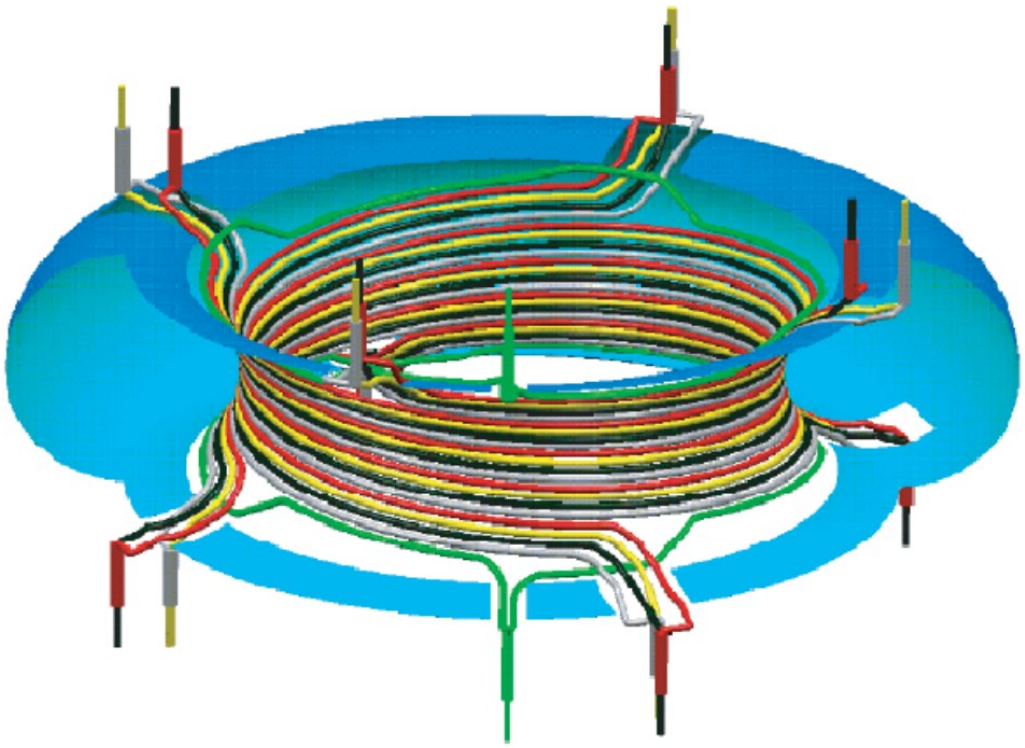

Figure 4 Representation of the DED coils in TEXTOR (Finken et al., 2004)

The magnetic coils represent one of the three vital components of a tokamak reactor, and the other two components are the first wall and the diverter. In figure 5, a cross sectional representation of ITER is given and the two components are highlighted. The first wall has the aim to create a chamber for the plasma and to protect the structural material from plasma exposure. It represents the focus of this work, so it is described in the following sections. On the other hand, the divertor represents the exhaust system of a tokamak and aims at removing helium ashes, heat, and other impurities from the plasma. The alfa particles

(helium) are produced during the fusion reaction at an energy (4.5 MeV) higher than the background plasma (~10 KeV), so once they cool down transferring their energy to the plasma they must be removed. They represent an impurity along with any other particle species that is not deuterium or tritium since they cool down the plasma causing its termination.

To solve the above issue, the magnetic configuration of a tokamak is designed in such a way that most of the interactions between the plasma and the PFCs take place at the divertor region whose material composition allows it to handle the particle flux and the heat loads coming from the plasma during the normal operation of a plasma. However, during off-normal events such as disruptions that lead to the REs generation all the tokamak structure is subjected to huge loads as described in the following sections.

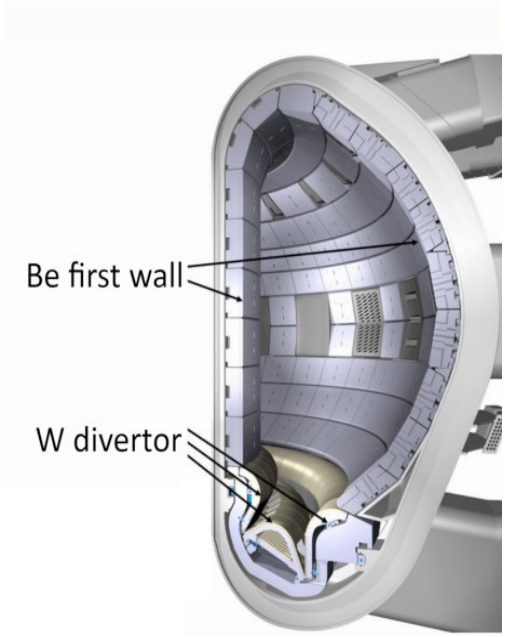

Figure 5 Cross sectional representation of a tokamak showing the plasma facing components (Cizek et al., 2019)

3. Runaway Electrons Impact

The REs has represented a problem since the starting of the fusion research, causing damage in multiple machines. In 1976, large runaway fluxes were reported in TFU 400 and Alcator, which led to the formation of holes into the vacuum chamber walls (TFR Group, 1980). In Doublet III during September 1981 runaway electrons damaged the graphite limiter as shown in figure 6 (Nishikawa et al., 1984). As it can be noticed the REs led to local damage of the limiter.

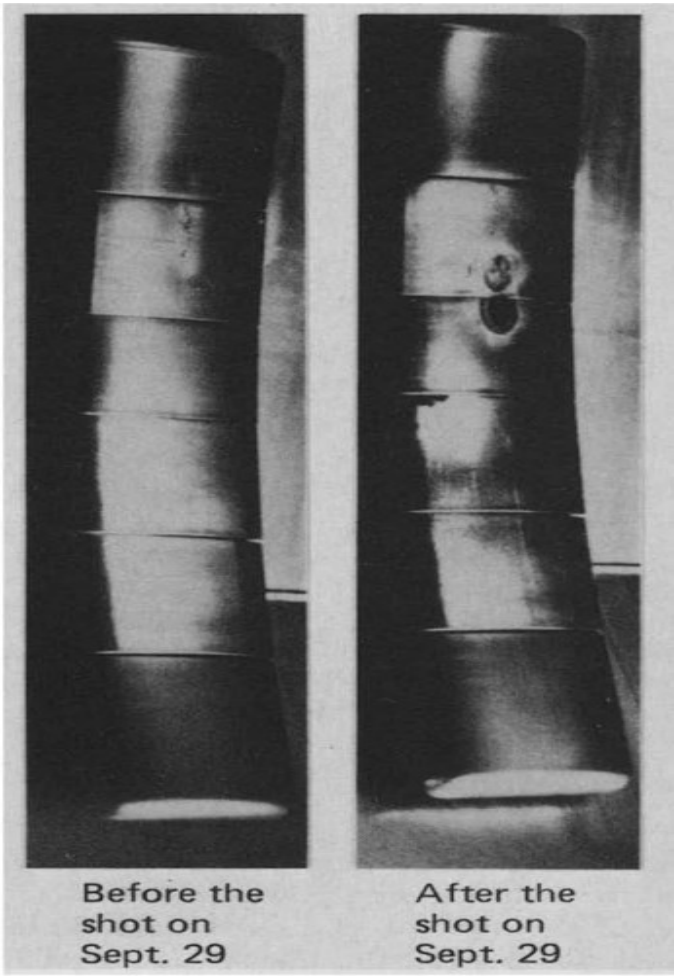

Figure 6 Surface damage on graphite limiter of Doublet III (Nishikawa et al., 1984)

In 1994, the Tora Supra outboard pump limiter was damaged by the REs generated during a disruption causing water leakage and activating the materials (Nygren et al., 1997).

These accidents have underlined that the generation of REs can take place in multiple situations in a Tokamak: at start up and during a plasma disruption (Russo et al., 1993). The most dangerous situation is represented by the

disruptions which can lead to the generations of REs with energies in the range of tens of MeV and carrying up to 60% of the plasma current.

The impact of the REs has been studied in the existing machines in two principal ways. The first is through accidental disruptions that cause local damage to the PFCs (Nygren et al., 1997) and the second are the provoked disruptions (Chen et al., 2012). The latter have been carried out in order to study the disruption mitigation systems, however, it has helped in understanding the nature of the REs impacting on the FW.

The impact of the runaway beam on the PFCs does not cause only a huge deposition of energy which leads to the melting, cracking, and evaporation of the material; it also leads to the production of photons and neutrons through (γ, n) nuclear reactions (Bolt et al., 1987). Therefore, the activation of the material takes place, requiring remote maintenance.

In JET, the runaway electrons caused the early replacement of the Inconel tiles, used for the protection of the central column of the machine, with the carbon tiles in 1984. Craters of up to 1 mm deep and having an area of 10 mm^2 were observed (Jarvis et al., 1988). Although carbon has a high melting point (strong sublimation at 3500 °C), which makes it adequate to be used as a protective material, the erosion of carbon by hydrogen chemical sputtering is very high. This, combined with the potential formation of hydro-carbons trapping a considerable amount of tritium in a future reactor, poses severe problems to the adoption of C as a suitable FW material. For this reason, the carbon tiles in JET have been replaced by the Beryllium ones.

The Beryllium (Be) FW will be used in ITER as well, since one of its benefits is a significantly reduced runaway production during disruption (Bartels, 1993). However, considering that in larger reactors, as reported in section 4, the avalanche mechanism will play a major role the Be first wall may have some issues in facing the REs problem. Indeed, Be has a lower melting point (1300 °C) with respect to the other candidate materials, which does not make it an optimal material to be used.

In the case of DEMO, Tungsten will be used for the first millimeters of the first wall since it has a higher melting point than Be (3400 °C). However, as shown in figure 7, the REs flux with an energy of 30 MeV could lead to grain growth and microcracking. The results in the figure were produced by irradiating a tungsten sample with electrons at 30 MeV and a duration of 30 seconds, to simulate the effects of several years of reactor operation (Bolt et al., 1987).

The mitigation of disruptions may also cause several problems related to the REs. The mitigation of disruptions with Argon does not lead to a damping of runaway current (Reux et al., 2015). In addition, in the case of mitigation with SPI, the fast energy removal can lead to additional REs generation as well (Bakhtiari et al., 2002). In figure 8, the damage caused by a failed mitigation attempt on Be tiles is

shown. Here, the JET Inner Wall Guard Limiter is hit by a beam over a 10 cm^2 area per tile (Reux et al., 2015).

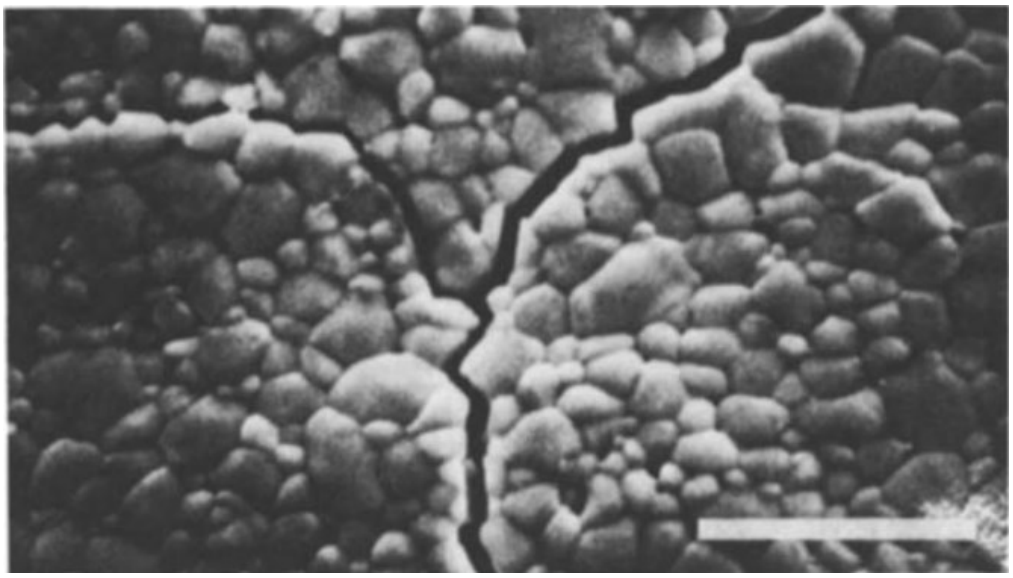

Figure 7 Surface of tungsten specimen after electron irradiation with 30 MeV for 30 s. The bar in the figure is 5 μm (Bolt et al., 1987)

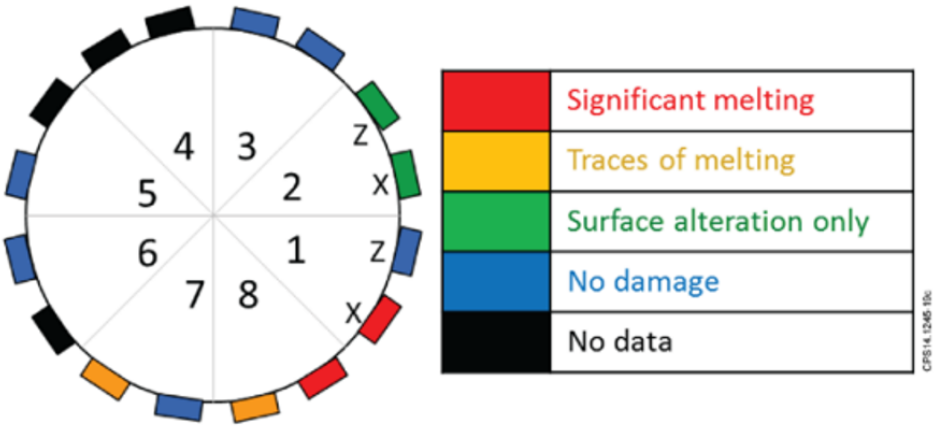

Figure 8 Tile damage on the JET inner wall guard limiter (top view, Octants number). The limiter consists of 16 toroidally distributed poloidal beams and they have been divided into octants (1-8). Each octant contains two beams that are called X and Z (Reux et al., 2015)

In figure 8, it can be noticed that not all the tiles were equally affected, two undergoing significant melting occurring mostly at a single toroidal location, while others places have experienced only some minor effects. In figure 9, the damage caused to the upper inner wall of JET can be observed.

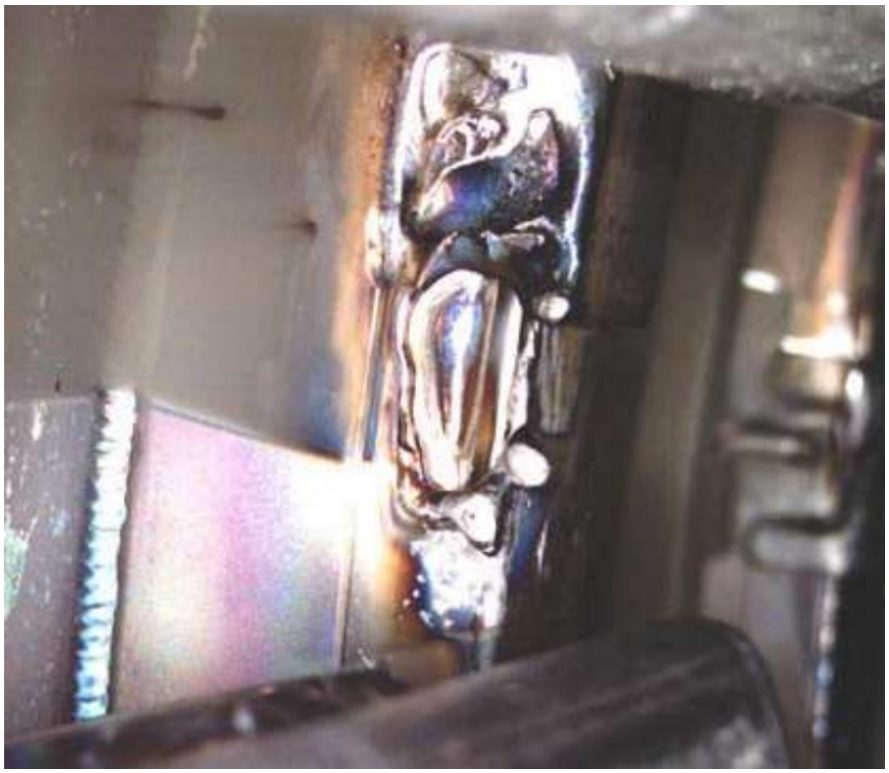

Figure 9 Melting damage to the JET upper inner wall (Fasoli, 2010)

The above description shows how the runaway electrons are problematic for current tokamaks. In the future ones, due to the higher energies involved, these problems will be even more severe. Noticeably, even the studied mitigation systems could lead to a generation of relativistic electrons in some cases, posing additional constraints on the design of efficient mitigation strategies. In order to have a better understanding of the REs behavior in different scenarios, the study of their generation mechanism is fundamental since it influences the efficacy of the selected mitigation systems.

4. Runaway Electrons Generation

The main process that leads to runaway electrons generation is related to the occurrence of disruptions in a Tokamak. A disruption leads to rapid and accidental termination of plasma, with huge thermal and mechanical loads on the structure. It is caused by the onset of a global instability, whose reasons can be multiple. Among other disruption-leading mechanisms, it is worth mentioning MHD instabilities and malfunctioning of control systems that causes a thermal quench of the plasma kinetic energy (Chen et al., 2012). In other words, it leads to the cooling of the plasma, increasing the plasma resistivity. The resistive plasma initiates the current quench, during which the confining poloidal magnetic field decays. Due to Faraday's law, the plasma tends to conserve the poloidal flux, and this leads to the generation of a strong toroidal electric field. A schematic representation of these events is given in figure 10 where the loss of thermal energy during the thermal quench and the loss of plasma current during the current quench can be observed along with the variation of the poloidal flux.

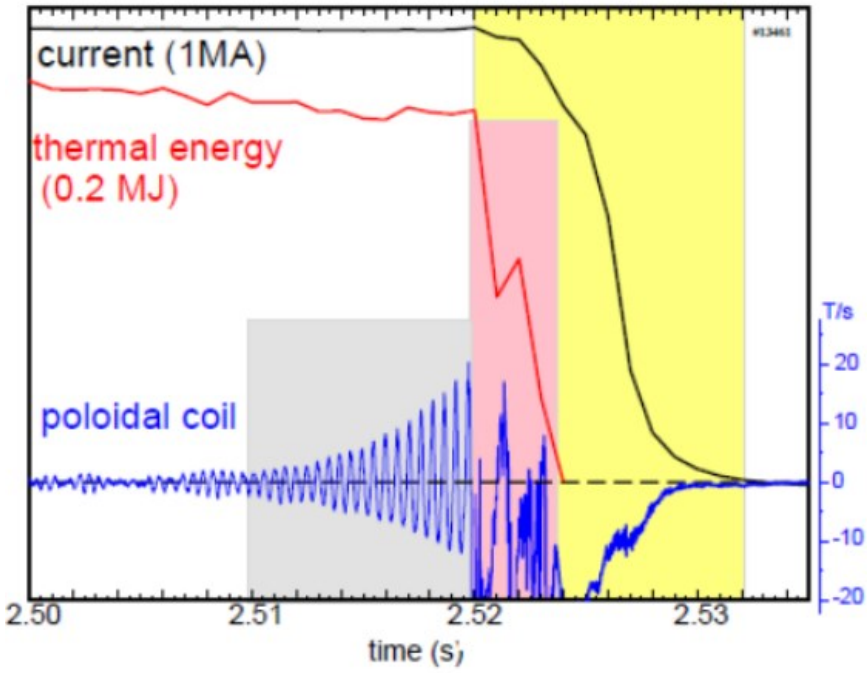

Figure 10 Representation of the different disruption phases: thermal quench (red), current quench (black) and variation of the poloidal magnetic field (blue) during JET shot 13461 (Siccinio, 2019)

In figure 10, it can be observed that once the disruption starts at 2.52 seconds there is an instant loss of thermal energy on a time scale of some milliseconds. The thermal quench causes an increase in the plasma resistivity causing a

reduction of the plasma current which in turn influences the poloidal magnetic flux. This leads to the generation of a toroidal electric field which translates into the acceleration of the electrons that acquire high energies which can carry up a large fraction of the plasma current as can be observed in subsection 4.3.

Equation (3) explains the acceleration of the electrons and shows the electron Coulomb collision frequency, considering an impact on particles of possible different species (labeled with the *k* index). Since the electron Coulomb collision frequency decreases as v_e^{-3}, it follows that electrons with energies larger than a critical threshold are continuously accelerated, entering the runaway domain (Fasoli, 2010)

$$\nu_{E_k}^{e/k} \sim n_k \frac{Z_e^2 Z_k^2 e^4}{2\pi\varepsilon_0^2} \frac{\ln\Lambda}{m_e m_k v_e^3} \tag{3}$$

In equation (3), particles of the species k can be ions or electrons, n_k is the particle k density, Z_k its charge, Z_e electron charge, ϵ_0 vacuum permittivity, $\ln\Lambda$ Coulomb logarithm which lies between 15 and 20 for quite all the fusion reactors (Freidberg, 2007), m_e the electron mass, m_k the k species mass and v_e is the electron velocity.

4.1. Dreicer Mechanism

The above phenomena, which represent the primary generation of the REs, can be explained in figure 11. The figure reports the collisional drag force F_c acting on electrons as a function of the relative velocity v_d between electrons and ions.

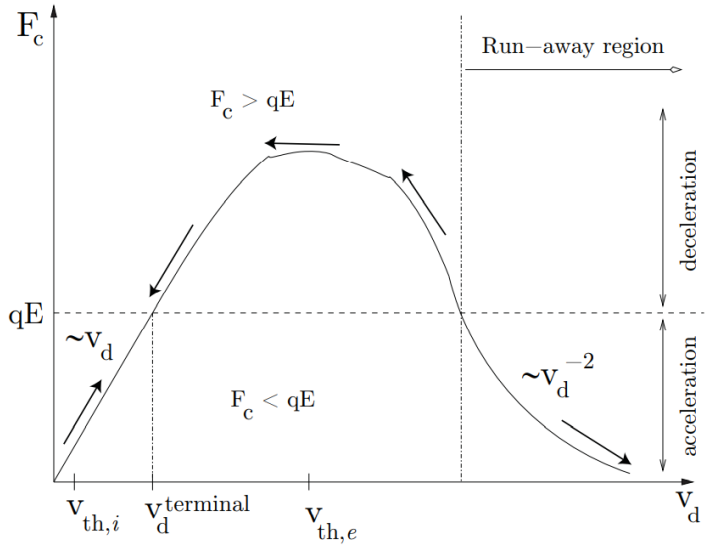

Figure 11 Collisional drag force acting on electrons vs electron velocity (Fasoli, 2010)

From figure 11, it can be noticed that when the drag force resulting from the collisions between electrons and ions, which causes the deceleration of the electrons, is larger than the term qE responsible for the acceleration of electrons, the two species converge to a certain velocity v_d. However, once the electric field is larger than a critical field, electrons reach the runaway region where they undergo an acceleration instead of deceleration. This happens when for a certain electron temperature, a critical electric field called the Dreicer field is reached. The Dreicer field is given by the equation (4).

$$E_D = \frac{n_e e^3 \ln\Lambda}{4\pi\varepsilon_0^2 T_e} \tag{4}$$

Where the electron temperature is,

$$T_e = \frac{1}{2} m_e v_d^2 \tag{5}$$

If the speed needed for the electron to run away is close to the light speed, a correction is made to the Dreicer field and the expression of the electric field becomes (Reux et al., 2015),

$$E_c = \frac{n_e e^3 \ln\Lambda}{4\pi\varepsilon_0^2 m_e c^2} \tag{6}$$

As it can be observed in expression (4) the Dreicer field is proportional to the ratio of the electron density and the electron temperature, the radial profiles of these two parameters are critical in generating the runaway electrons (Kawamura et al., 1989). Due to this dependence, the runaway electrons can be generated in any plasma region, however, only those originating in the central region will remain confined enough to acquire higher energies and damage the machine structure.

4.2. Avalanche mechanism

The study of the REs generation has been carried on multiple machines like JET, JT-60U, Tore Supra, TEXTOR, etc. and simulations have been done also for future machines like ITER and DEMO. Unlike, the existing machines where the main process of REs generation is the Dreicer mechanism, which is described above, in future machines, the avalanche mechanism is thought to create major issues.

The avalanche mechanism consists of an exponential growth of the runaway electron population. Since at higher energies the drag force acting on the electrons decreases rapidly and the collision events reduce drastically, these particles travel larger distances, and the presence of the toroidal electric field leads to their acceleration. Along their path, they undergo close Coulomb collisions with the background plasma electrons causing the generation of secondary electrons that accelerate to higher energies continuing the avalanche process (Jayakumar et al., 1993). The effect of the avalanche mechanism on the

runaway current can be observed in figure 12 where the runaway current observed in JET is shown with and without avalanche mechanism.

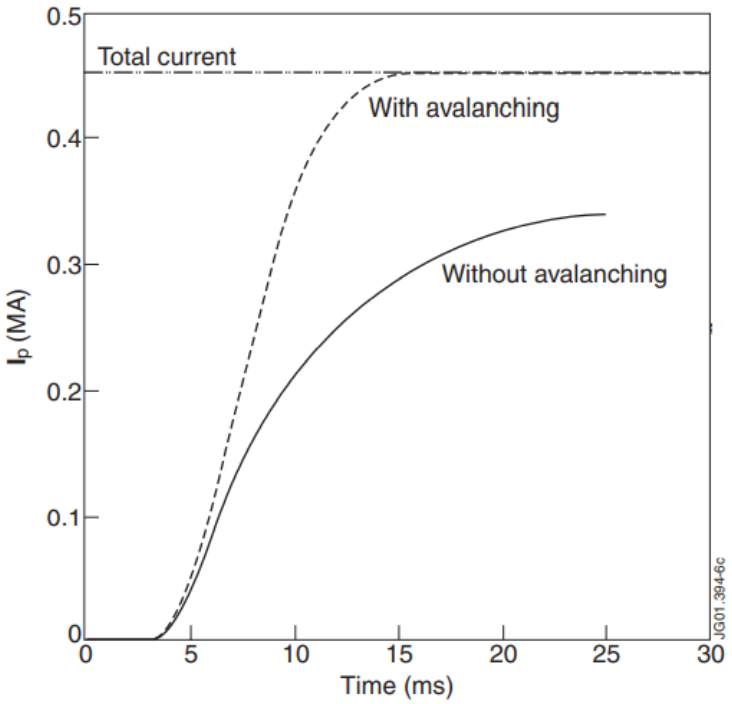

Figure 12 Runaway current evolution observed in JET with (dashed line) and without (black line) avalanche (Gill et al., 2002)

Noticeably, the avalanche mechanism leads to a large increase in the runaway current, and this mechanism would be the main responsible for the REs generation in the future tokamaks because, in large reactors, the plasma current is much higher than the current ones. To explain it better, the growth rate of REs due to the avalanche mechanism (γ_{RA}) is considered (Rosenbluth et al., 1997),

$$\gamma_{RA} = \frac{1}{j_{RA}}\frac{dj_{RA}}{dt} \approx \frac{eE}{2mc\ln\Lambda} \tag{7}$$

Where j_{RA} and the derivative represent the runaway current and its growth rate due to avalanche, m is the mass of electrons, c is the light speed, $\ln\Lambda$ is the Coulomb logarithm, e is the electron charge and E is the toroidal electric field. The reason for the second equality is that at high loop voltage, the γ_{RA} is proportional to the toroidal electric field (Jayakumar et al., 1993). Moreover, in a disruption, the loop voltage is produced by the decay of the plasma current, and this enables to estimate the e-folds growth during the avalanche mechanism (Rosenbluth et al. 1997),

$$\gamma_{RA} t \approx \exp\left(\frac{eEt}{2mc\ln\Lambda}\right) \approx \exp\left(\frac{I_p}{I_A ln\Lambda}\right) \tag{8}$$

where I_P is the plasma current and I_A is the Alfven current (Ding et al., 1999) computed as (Putvinski et al., 1997),

$$I_A = \frac{mc^3}{e} \approx 0.02 \text{ MA} \quad (9)$$

Since the Alfven current and the Coulomb logarithm, the latter assumed to be in the range 15-20, are constant the growth rate depends on the plasma current. In the current reactors, the plasma current is around 1 MA which gives an amplification factor due to the avalanche of e^2, but in ITER and DEMO where the involved plasma currents are much higher, the avalanche amplification of runaway will be greater than e^2. For ITER this factor can reach values up to e^{50} if I_P=15 MA and $\ln\Lambda$ = 15 are considered, causing the avalanche mechanism to become the primary mechanism for runaway generation(Fülöp et al., 2013).

At the same time, Beryllium (Be) FW will be used in ITER since one of its benefits is a significantly reduced runaway production during disruption, as it has been demonstrated in JET-ILW (ITER Like Wall) (Bartels, 1993). The reason behind the absence of REs is related to a slower current quench which in turn is explained by the lower radiation losses of the plasma in absence of the carbon as a radiating impurity. In other words, the lower cooling rate of Be in the current quench temperature range translates into a hotter plasma, slowing down the current quench. A slower current quench means a lower accelerating toroidal electric field, finally leading to less runaway generation (Reux et al., 2015).

4.3. Influence of Plasma Parameters on REs Generation

In addition, it has been demonstrated in the current machines that the generation of runaways depends also on some other parameters, such as the toroidal magnetic field and the plasma current. Moreover, a vertically unstable plasma does not experience a significant runaway current as the plasma hits the wall before a significant runaway current is formed (Lehnen et al., 2009).

In J-TEXT tokamak the influence of the toroidal magnetic field and the plasma current on the runaway electrons generation has been studied (Chen et al., 2012). As it can be noticed in figure 13, a toroidal magnetic field lower than 2.2 T does not generate runaway electrons during a disruption. In general, a limit of 2 T is valid for most current machines, and the reason for this threshold is thought to be linked to the Whistler waves that are excited by REs (Fülöp et al., 2013). These waves can be destabilized by REs and the growth rate of these unstable waves is inversely proportional to the strength of the magnetic field, and they may stop or reduce the runaway generation by the avalanche mechanism causing a rapid pitch-angle scattering of the REs. However, this explanation is still under investigation, and it is still to be validated. Moreover, in larger reactors with

higher toroidal fields the probability of having runaways increases, with a tendency of having higher runaway currents (Lehnen et al., 2009).

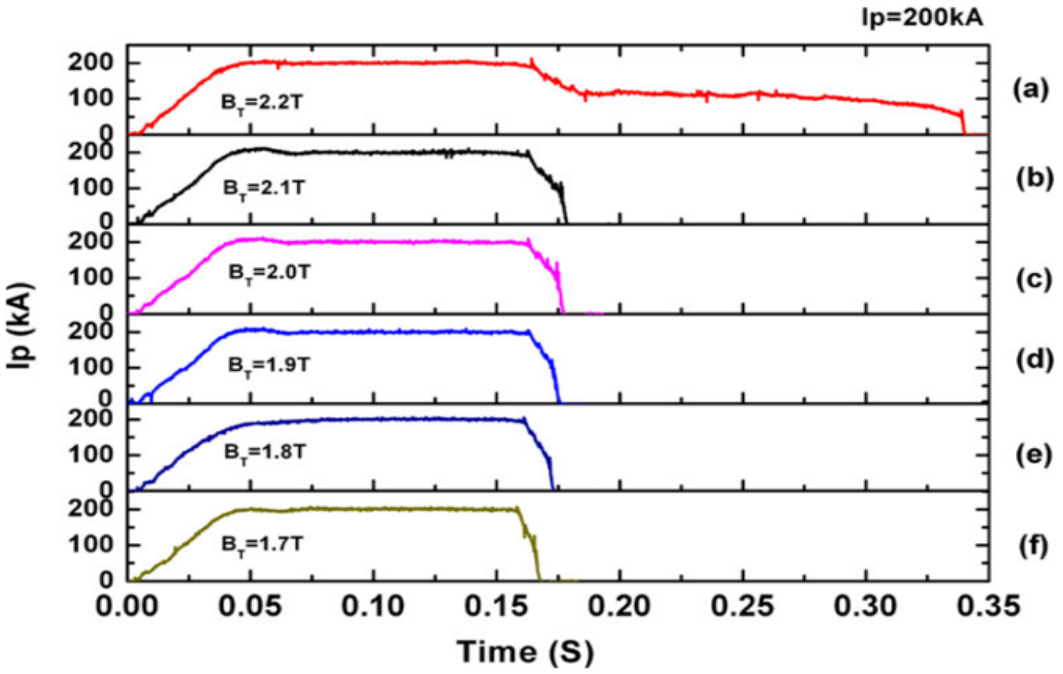

Figure 13 Plasma current termination at different toroidal fields (Chen et al., 2012)

At a certain toroidal field, the plasma current plays a role in the REs generation as well. In figure 14, the current waveform at different plasma currents and fixed toroidal magnetic fields are reported.

With respect to the behavior with different toroidal magnetic fields, in figure 14 it can be observed that there seems not to exist a minimum plasma current value allowing the generation of runaway electrons. Plasma currents larger than a certain value, which for J-TEXT is 200 kA and for JET 2 MA, do not lead to REs generation due to magnetic fluctuations which prevent their production. At lower plasma currents the life of the runaways varies with the current value itself, and the runaway current plateau is lost early (Chen et al., 2012). Moreover, the degree of conversion of pre-disruptive plasma current in runaway current is influenced by the actual current level (Lehnen et al., 2009).

Once generated, the runaway current terminates on the FW of the machine, damaging the structure. As discussed above, in larger machines like ITER and DEMO, the probability of runaway current generation is higher and the amount of damage that can be caused to the structure represents a serious threat to their reliable operation. Consequently, the design and testing of REs suppression and mitigation systems are essential.

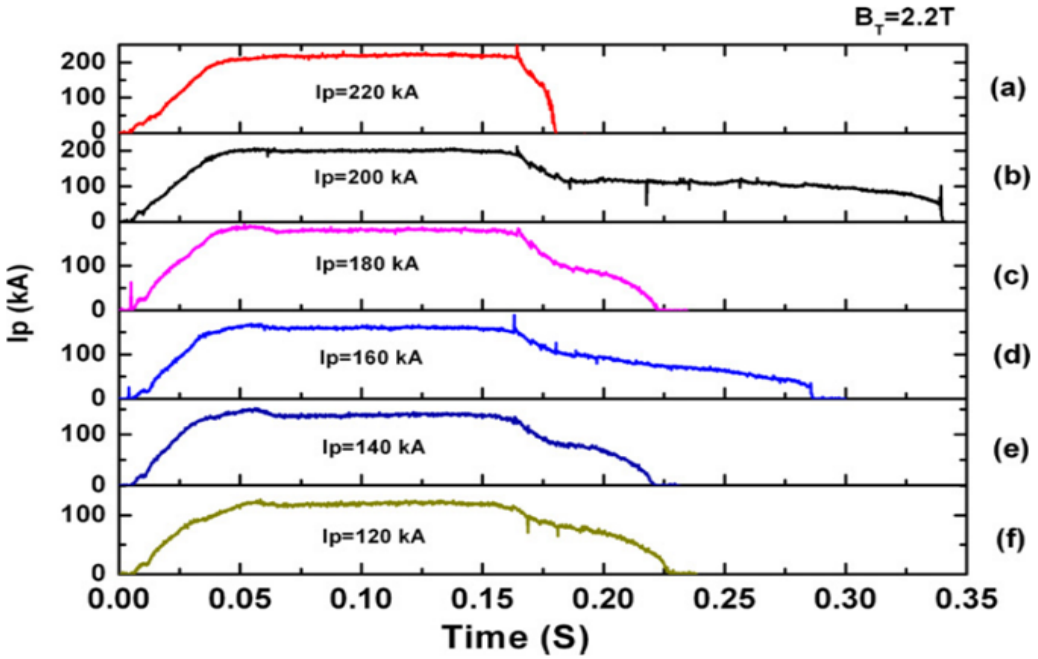

Figure 14 Plasma current termination at different plasma currents and fixed toroidal magnetic field (Chen et al., 2012)

5. Runaway Electrons Suppression and Mitigation

Multiple systems are under study to mitigate the effect of disruptions and REs. In particular, Massive Gas Injection (MGI), Shattered Pellet Injection (SPI), Resonant Magnetic Perturbation (RMP), and Magnetic Energy Transfer (MET). In this section, these four systems will be briefly described, in order to explain how they help to mitigate or suppress the runaway electrons.

5.1. Massive Gas Injection and Shattered Pellet Injection

The MGI system is the most used disruption mitigation system in the current tokamaks and is thought to be present in future reactors as well. Different gasses have been used for this system to increase the plasma density and cool it down by radiation. As it can be observed in expression (6), an increase in the electron density would lead to a higher threshold electric field necessary for the runaway electron generation (Bozhenkov et al., 2008). However, a complete suppression cannot be obtained since it would require injecting large quantities of impurity gas which may affect the vacuum system (Cai et al., 2021).

MGI systems using only argon (Ar) as impurity gas leads to a fast shutdown of the plasma, however, Ar leads to the generation of runaway electrons, due to its poor mixing efficiency (Bozhenkov et al., 2008). The mixing efficiency, defined as the ratio between the number of atoms able to reach the core of the plasma and the number of atoms injected before the disruption, is only 3% for Ar. The presence of Ar atoms leads to the generation of REs through the interaction of REs generated by the Dreicer mechanism and Ar that have not reached the core of the reactor. That is along their path, the REs can encounter argon atoms causing the generation of secondary electrons that accelerate to higher energies continuing the avalanche process. A schematic representation of this process is shown in figure 15 where the electrons interact with the Ar atoms producing ions and electrons that are further accelerated to the relativistic energies.

Ar being a high Z impurity increases the radiation losses, but at the same time, it leads to the generation of REs. On the other hand, deuterium (D) injection leads to a much lower runaway generation thanks to its rapid mixing in the plasma due to its high sound speed, but the shutdown time is much larger. As a consequence, a mixture of argon and deuterium is used in the current reactors where Ar radiates the plasma energy and D increases the plasma density to avoid REs generation (Reux et al., 2015). In this way, the runaway electron generation is partly suppressed or mitigated in the Dreicer mechanism which is the primary generation mechanism in the current reactors and the presence of argon does not strengthen the avalanche mechanism due to its limited amount. Indeed, the mixture consists of 90% D + 10% Ar (Reux et al., 2015).

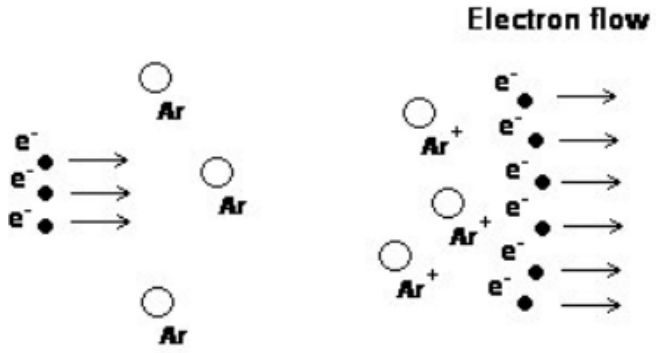

Figure 15 Schematic representation of the interaction between electrons and Ar atoms (Kemaneci, 2009)

However, in ITER and DEMO, the avalanche mechanism will be the main issue and currently, it is not fully clear how the generation under this mechanism will be suppressed. Indeed, in order to avoid the avalanche mechanism in ITER, an injection of 10^{25} atoms is required and this could impact the vacuum systems. At the same time, densities required to suppress the avalanche mechanism have not been reached in the current reactors (Lehnen et al., 2008).

For the SPI system, high-speed neon ice pellets have been used in many of the current reactors (Bakhtiari et al., 2002). The pellets injected in the main chamber ablate and evaporate cooling down the plasma (Breizman et al., 2019). In general, this system leads to a rapid shut down of the plasma, nevertheless, it can also cause the generation of runaway electrons. This is caused by the presence of a residual hot electron tail after a rapid cooling of the plasma. Since, overall, the pellet causes a rapid reduction in the electron temperature which translates into a higher resistive electric field in the plasma, this electric field may overcome the critical field and leads to the runaway generation (Chen et al., 2012).

5.2. Resonant Magnetic Perturbation and Magnetic Energy Transfer

The RMP system consists in using external coils to suppress or mitigate the runaway electrons by enhancing their radial losses through the induction of suitable magnetic perturbations in the plasma. Its use has been demonstrated in multiple reactors like JT-60, TEXTOR, etc. In figure 16, the impact of this system on the runaway current can be observed for TEXTOR. For this experiment, the disruption is triggered at 2 seconds with massive argon injection that causes the generation of a runaway electron current measured by the electron cyclotron emission (ECE) diagnostic for energies below 3 MeV, and by the infrared camera for energies up to 25 MeV (Lehnen et al., 2008).

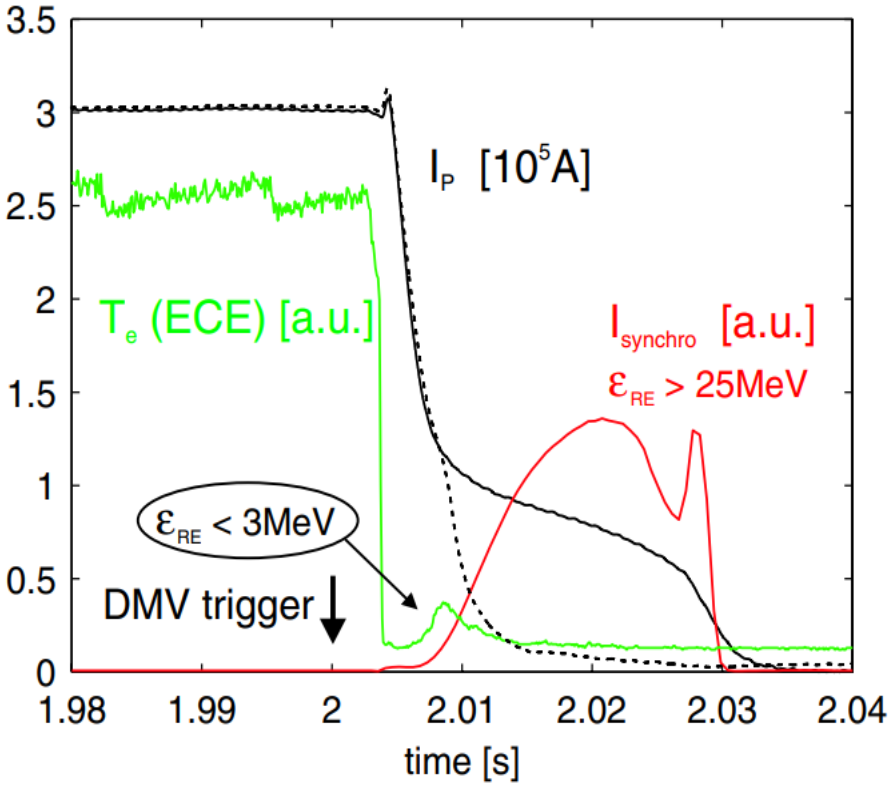

Figure 16 Evolution of the plasma current Ip (black) and electron temperature Te (green) during disruption. After 2 seconds the runaway current is measured by ECE (red) and infrared camera. The dashed black line is the Ip with RMP (Lehnen et al., 2008)

After the thermal quench, the current quench takes place, which can generate a runaway current with a plateau that can live up to 50 ms. The dashed line in figure 16 shows the influence of the RMP produced by the coils of the dynamic ergodic divertor (DED). It has been demonstrated experimentally that with a perturbation amplitude of toroidal mode number n=2 a strong suppression of the runaway current is possible. However, a *complete* suppression cannot be achieved, and this system works only for the avalanche mechanism (Lehnen et al., 2009). The reason for this is related to the fact that the runaway generation due to the Dreicer mechanism increases exponentially with the electric field and cannot be compensated using the RMP system (Lehnen et al., 2009).

At the same time, the large size of the future tokamaks like ITER and DEMO would increase the distance between the RMP coils and the plasma core, leading to an additional problem in suppressing the runaway electrons (Cai et al., 2021).

The MET has been developed recently for REs suppression in J-TEXT. This system aims at reducing the toroidal electric field which is developed during the current quench phase by transferring the plasma poloidal magnetic energy out of the vacuum vessel through the use of energy transfer coils (Cai et al., 2021). In

figure 17, the design of this system, based on magnetic coupling, used in J-TEXT is shown.

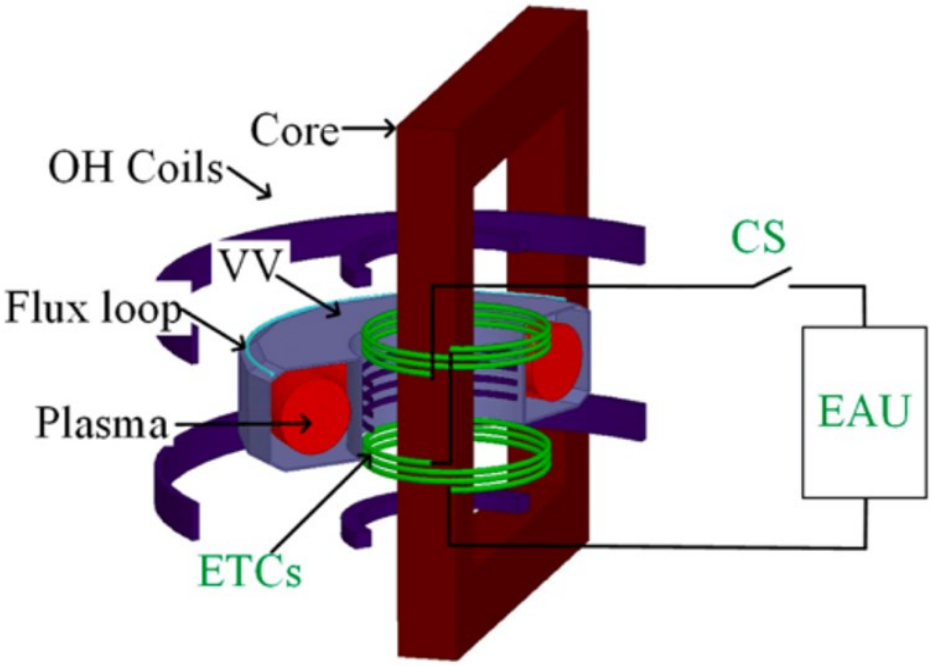

Figure 17 Schematic representation of MET in J-TEXT (Cai et al., 2021)

As the coils for the energy transfer are magnetically coupled with the magnetic field in the plasma, during the plasma current decay phase a current is induced in these coils. This leads to the coupling of a fraction of the poloidal magnetic energy to the ETCs, which will be transferred out of the Vacuum Vessel if the controlling switch (CS) is triggered and will be consumed in the energy absorbing unit. Thanks to the use of this system, around 20% of the poloidal magnetic energy can be reduced during a disruption. This lowers the toroidal electric field which influences the runaway generation. For a better understanding, in figure 18, the influence of the MET system during a provoked disruption in J-TEXT is presented, compared with the disruption evolution in absence of such a system.

Even in J-TEXT, the provoked disruption is implemented using the Ar injection (occurring at $t=0.4$ s). As it can be observed, with MET there is a suppression of the runaway current with a current induced in ETCs (I_{ETC}). The reduced toroidal field and loop voltage lead to a runaway current of 30 kA and the runaway plateau was not observed which leads to a higher loss rate of runaway as can be noticed by the hard x-ray signal (Cai et al., 2021).

However, it is a new system that has been used only in J-TEXT where there is no risk to have toroidal eddy currents in the Vacuum vessel which favor the

magnetic coupling. As a consequence, it has to be further investigated in order to be a part of the ITER disruption mitigation system.

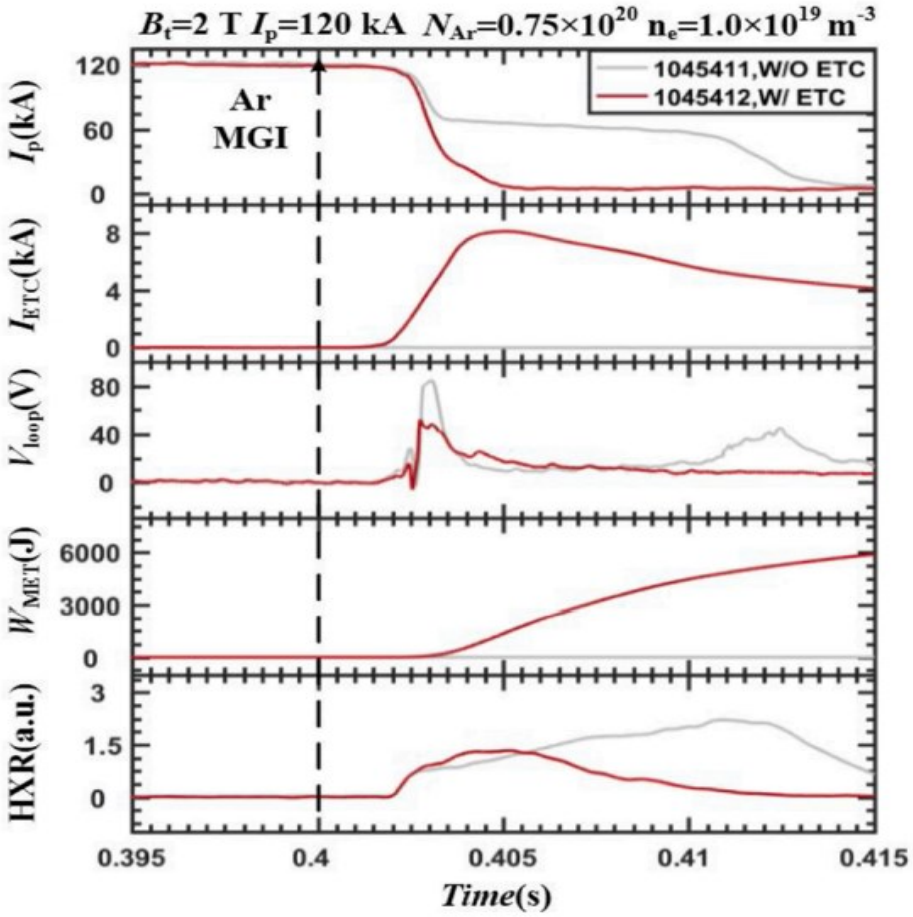

Figure 18 Experimental results for REs suppression with MET (grey curves) in J-TEXT (Cai et al., 2021)

6. Overview of the FLUKA code

FLUKA is a multipurpose Monte Carlo code used to compute the energy deposition on the DEMO FW and to implement the REs beams observed for some shots in JET, in this study. It has been developed at CERN in collaboration with INFN, and it simulates the transport and interaction of several nuclear particles with matter (Ballarini et al., 2006). In particular, the code can simulate electrons interactions, photon interactions, particle decay, etc and it has been already applied for runaway energy deposition analysis in ITER-FEAT PFCs (Federici, 2019).

FLUKA can study the interaction and propagation of around 60 particle species in matter with high accuracy. In particular, photons and electrons are traced in an energy range that goes from 100 keV to thousands of TeV, along with neutrons starting from thermal energies. It has been applied in different fields like calorimetry, dosimetry, detector design, and shielding.

The code is written in the Fortran 77 programming language and for most applications, no specific language skills are required for the users. However, the advanced user can interact with several user-interface routines provided to allow defining some specific features like, e.g., particular sources or estimators. This provides increased flexibility, at the obvious cost of at least some programming skills. Also, special attention is given to the representation of the studied geometry by the user through a combinational Geometry package.

One of the advantages of FLUKA with respect to other Monte Carlo codes is that, thanks to the use of a multiple Coulomb scattering algorithm, the simulation results are independent of the step length (Maddaluno et al., 2003).

For non-expert users, the use of the FLUKA code could be relatively complicated as it does not have a user-friendly interface as shown in figure 19. In the figure, the definition of the particle source and the geometry is shown without any additional suggestions about the meaning of the different inputs for which the user is asked to refer to the code manual. Moreover, the use of additional user routines needed to personalize a source, or a detector, is difficult to add in this mode of FLUKA.

For this reason, an advanced interface called FLAIR has been paired with FLUKA. Figure 20 represents the main tabs of the program each having its own features.

The interface is based on python language with C++ extension used for the geometry visualization. Thanks to this feature it is possible to design the geometry interactively by visualizing the designed system in real-time. In addition, the user routines are easier to set in the working environment.

```
TITLE
My Basic Input example
* Set the defaults for precision simulations
DEFAULTS                                                              PRECISIO
* Define the beam characteristics
* ..+....1....+....2....+....3....+....4....+....5....+....6....+....7..
BEAM              3.5 -0.082425       -1.7        0.0        0.0          PROTON
* Define the beam position
* ..+....1....+....2....+....3....+....4....+....5....+....6....+....7..
BEAMPOS           0.0        0.0       -0.1        0.0        0.0
*
GEOBEGIN                                                              COMBNAME
    0     0
* Black body
SPH blkbody     0.0 0.0 0.0 100000.0
* Void sphere
SPH void        0.0 0.0 0.0 10000.0
* Cylindrical target
RCC target1     0.0 0.0  0.0 0.0 0.0 10.0 5.0
RCC target2     0.0 0.0 20.0 0.0 0.0 10.0 5.0
RCC target3     0.0 0.0 40.0 0.0 0.0 10.0 5.0
END
* Black hole
BLKBODY       5 +blkbody -void
* Void around
VOID          5 +void -target1 -target2 -target3
* Target
TARGET1       5 +target1
TARGET2       5 +target2
TARGET3       5 +target3
END
GEOEND
```

Figure 19 FLUKA interface without the use of a graphical interface

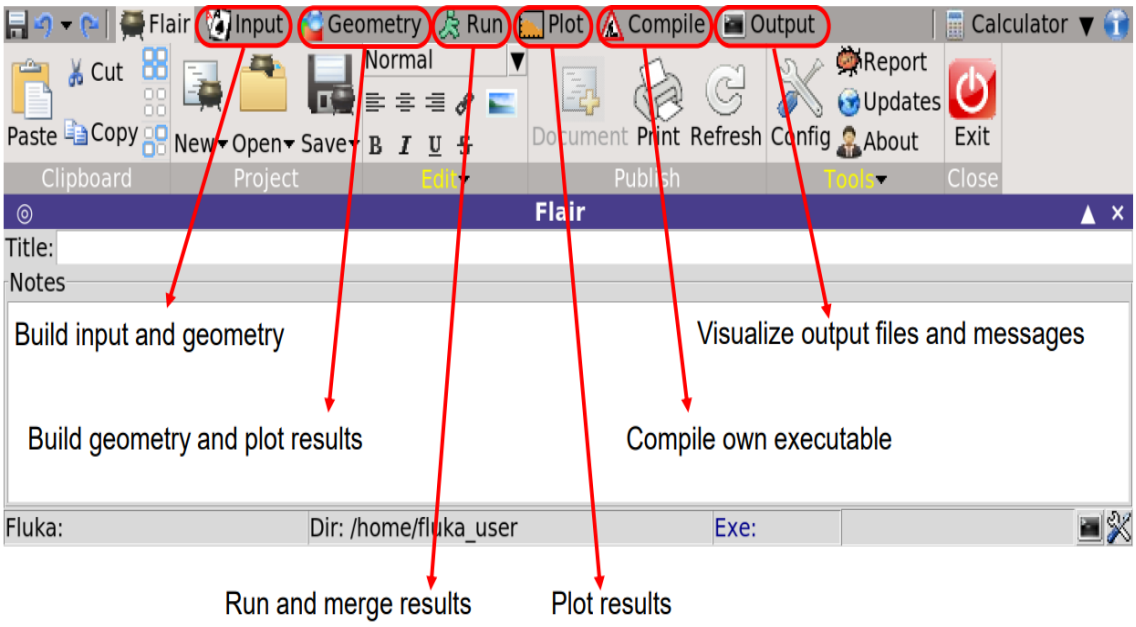

Figure 20 Representation of the FLAIR interface

6.1. Steps of a FLUKA run

In order to run a simulation in FLUKA the user have to define the number of *primary* particles. These particles are called primary to distinguish them from any

secondary particles that are generated through interaction with matter. The next step consists in defining the number of cycles. In FLUKA, the total number of particles is divided into a finite number of cycles to obtain accurate results (further details in subsection 6.3.). For instance, if a simulation is made of 1e6 particles and 5 cycles are defined, each cycle will consist of a simulation of 2e5 particles.

During the simulation of a cycle, each particle undergoes the following sequence of steps:

1. Each particle is loaded in a stack with all of its properties. A stack consists in a set of arrays containing the needed information about the particle, that is position, incidence angle, statistical weight, etc (FLUKA, 2020).
2. The code checks the position of the particle, if it is positioned in the region called Vacuum it is transported to the material boundary. The vacuum region consists in one of the two mandatory regions that surround the user defined geometry. For further details see subsection 7.3.1.
3. Once the material is reached, FLUKA computes the total interaction cross section of the particle at its energy and the material. This cross section σ consists in the probability of the particle undergoing an interaction
4. The computed cross section is used to define the mean free path to the next interaction through (10)

$$\lambda = \frac{1}{N\sigma} \tag{10}$$

   Where N is the number of scattering centers per unit volume in a medium. The mean free path is the distance traveled by the particle between two successive interactions.
5. The computed mean free path is used to sample the step length between two interactions from (11)

$$p(s) = \frac{1}{\lambda}\exp\left(-\frac{s}{\lambda}\right) \tag{11}$$

   The sampling consists in the generation of random variables according to a given distribution and in FLUKA it is done by using multiple sampling techniques (FLUKA, 2020). At the same time, thanks to the features of FLUKA the final results are independent of the step length (Ferrari et al., 1992).
6. The nature of the interaction is defined through (12)

$$P_i = \frac{\sigma_i}{\sigma}, i = 1,2,..n \tag{12}$$

Where P_i is the probability of interaction i and σ_i is the cross section of interaction i and n is the total number of interactions the particle can undergo.

7. For the i-th selected mechanism, the energy lost by the particle and the change of direction are sampled through the differential cross section of mechanism i.
8. The energy lost by the particles and the change of direction are saved in an estimator.

Once this sequence is completed, it is repeated from the step 2 if the energy of the particle is above a threshold defined by the user, or the particle has not escaped from the geometry. If these two conditions are not satisfied, the code passes to the next particle of the cycle.

Once the cycle is completed, the results are saved in an output file and the next cycle is started assuming the properties of the material to be unchanged with respect to their starting properties (FLUKA, 2020). That is if the second cycle of particles is initiated the code does not consider that the properties of the materials may have been changed after cycle 1. If 5 cycles are simulated this would mean 5 different result files.

In this way, n output files are generated with n equal to the number of cycles as shown in figure 21. In figure, the number of cycles is assumed to be equal to 5.

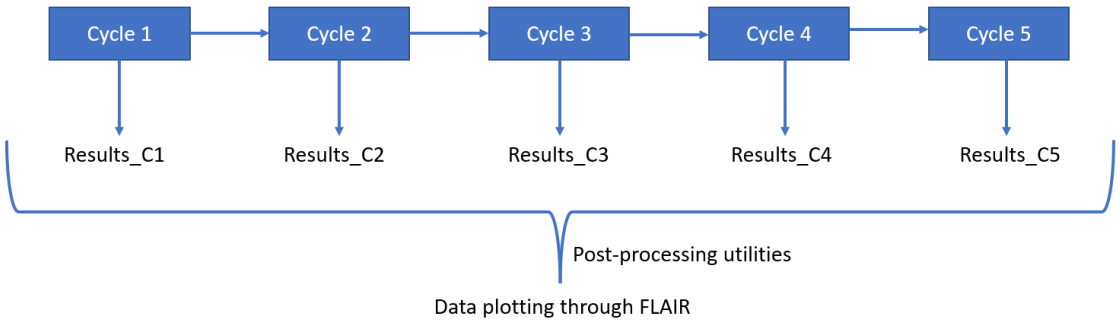

Figure 21 Steps for data representation

In figure 21, 5 cycles give 5 results files containing a summary of the input variables and the output required by the user. This output can be the energy deposition, particle fluence, etc. (FLUKA 2020). In order to have a single set of results instead of 5 different files, FLUKA merges all the results using post-processing utilities embedded in the code in 1 output file which contains the desired output for the total number of primaries (2e5 x 5 = 1e6 particles for the example above) and the associated uncertainties. This final output file which has the form shown in figure 22 is handled by FLAIR in order to represent the results

according to the needs of the user. For this study, these results are represented in subsection 7.3.

6.2. Energy deposition scoring

The energy deposition is scored using built-in scoring methods of FLUKA which allows computing the energy deposition through the geometry binning option. The latter consists in the definition of a regular spatial mesh that divides the geometry defined by the user in a certain number of bins along the 3 directions (x,y,z) in order to have a good visualization of the results. The resolution of the plots increases with the number of bins and the maximum number of bins that can be defined by the user are 400.

The estimator used in this study is called USRBIN and it computes the spatial distribution of the energy density over a region defined by the user. The results of this estimator are given in the form of a 3D matrix where the data are written as a 1D sequence of total length NX×NY×NZ, where NX, NY, NZ are the number of bins in the x, y, and z directions, respectively. To explain it better, in figure 22 the 3D matrix is shown where in the beginning the number of the bins in each direction is reported. Being the number of bins equal to 320 for X and Y direction, it is a 320x320 matrix and the number of columns is fully arbitrary since it is a 1D sequence.

```
X coordinate: from  1.6000E+01 to  2.4000E+01 cm,   320 bins ( 2.5000E-02 cm wide)
Y coordinate: from  1.9975E+01 to  2.0025E+01 cm,     1 bins ( 5.0000E-02 cm wide)
Z coordinate: from -4.0000E+00 to  4.0000E+00 cm,   320 bins ( 2.5000E-02 cm wide)
Data follow in a matrix A(ix,iy,iz), format (1(5x,1p,10(1x,e11.4)))

accurate deposition along the tracks requested

 0.0000E+00  0.0000E+00  0.0000E+00  0.0000E+00  0.0000E+00  0.0000E+00  0.0000E+00  0.0000E+00  0.0000E+00  0.0000E+00
 0.0000E+00  0.0000E+00  0.0000E+00  0.0000E+00  0.0000E+00  0.0000E+00  0.0000E+00  0.0000E+00  0.0000E+00  0.0000E+00
 0.0000E+00  0.0000E+00  0.0000E+00  0.0000E+00  0.0000E+00  0.0000E+00  0.0000E+00  0.0000E+00  0.0000E+00  0.0000E+00
 0.0000E+00  0.0000E+00  0.0000E+00  0.0000E+00  0.0000E+00  0.0000E+00  0.0000E+00  0.0000E+00  0.0000E+00  0.0000E+00
 0.0000E+00  0.0000E+00  0.0000E+00  0.0000E+00  0.0000E+00  0.0000E+00  0.0000E+00  0.0000E+00  0.0000E+00  0.0000E+00
 0.0000E+00  0.0000E+00  0.0000E+00  0.0000E+00  0.0000E+00  0.0000E+00  0.0000E+00  0.0000E+00  0.0000E+00  0.0000E+00
 0.0000E+00  0.0000E+00  0.0000E+00  0.0000E+00  0.0000E+00  0.0000E+00  0.0000E+00  0.0000E+00  0.0000E+00  0.0000E+00
 0.0000E+00  0.0000E+00  0.0000E+00  0.0000E+00  0.0000E+00  0.0000E+00  0.0000E+00  0.0000E+00  0.0000E+00  0.0000E+00
 9.9621E-03  9.2244E-03  9.1173E-03  9.0000E-03  9.1993E-03  9.3541E-03  8.5903E-03  9.0893E-03  9.0300E-03  9.1253E-03
 9.7527E-03  9.0268E-03  8.9905E-03  9.4805E-03  1.0542E-02  9.6824E-03  9.9168E-03  9.9952E-03  1.0544E-02  9.9804E-03
 9.5659E-03  9.8463E-03  9.7429E-03  1.0161E-02  9.5033E-03  9.6727E-03  9.9479E-03  9.2306E-03  1.0300E-02  1.0502E-02
 1.0161E-02  9.2284E-03  9.2892E-03  8.7438E-03  8.3441E-03  8.8891E-03  9.6802E-03  9.3054E-03  9.6331E-03  9.3666E-03
 9.3443E-03  9.0316E-03  8.9109E-03  9.0514E-03  9.3484E-03  9.3855E-03  8.6047E-03  9.1949E-03  1.0111E-02  9.8467E-03
 9.4838E-03  9.9848E-03  9.4171E-03  9.3192E-03  9.1054E-03  1.0170E-02  9.9984E-03  9.7012E-03  9.2479E-03  8.9990E-03
 8.9693E-03  1.0018E-02  9.9285E-03  1.0194E-02  9.8013E-03  9.7326E-03  9.9607E-03  9.5183E-03  9.2752E-03  9.2912E-03
 9.2928E-03  9.3788E-03  9.4480E-03  9.8072E-03  9.4954E-03  9.3605E-03  9.7895E-03  9.8785E-03  1.0042E-02  9.6290E-03
 1.0279E-02  1.0316E-02  1.0368E-02  9.5499E-03  8.9856E-03  9.0699E-03  9.4033E-03  9.6735E-03  9.4913E-03  9.6034E-03
 9.1389E-03  9.2164E-03  9.3424E-03  9.7770E-03  9.2740E-03  9.3293E-03  9.6848E-03  9.0673E-03  9.6079E-03  9.1454E-03
 9.5151E-03  9.7180E-03  1.0318E-02  1.0290E-02  9.5011E-03  8.9671E-03  8.9377E-03  9.7995E-03  9.8927E-03  9.7880E-03
 1.0068E-02  9.4725E-03  1.0435E-02  9.5886E-03  1.0021E-02  9.7363E-03  9.6342E-03  9.7180E-03  9.0855E-03  9.0026E-03
 8.5205E-03  9.2006E-03  9.7494E-03  9.8139E-03  9.5108E-03  9.0916E-03  8.7918E-03  8.8261E-03  1.0055E-02  9.4462E-03
 8.9080E-03  9.0411E-03  9.1528E-03  9.5628E-03  9.7675E-03  1.0051E-02  1.0571E-02  1.1135E-02  1.0711E-02  1.1174E-02
 1.1238E-02  1.0045E-02  9.5235E-03  9.7491E-03  9.7203E-03  1.0796E-02  1.0460E-02  1.0322E-02  9.5104E-03  9.7617E-03
 9.7682E-03  1.0739E-02  1.0477E-02  9.8272E-03  9.4060E-03  9.7636E-03  1.0023E-02  1.0294E-02  1.0008E-02  1.0068E-02
 1.0200E-02  1.1066E-02  1.0455E-02  1.0024E-02  9.3675E-03  9.3248E-03  9.0957E-03  9.6407E-03  9.9967E-03  9.2074E-03
 9.5686E-03  9.2416E-03  9.5278E-03  9.9118E-03  9.6209E-03  9.9239E-03  9.7269E-03  1.0025E-02  1.0164E-02  1.0084E-02
 1.0194E-02  9.6456E-03  9.5257E-03  9.6932E-03  9.6061E-03  9.9270E-03  9.8421E-03  1.0351E-02  1.0568E-02  9.7561E-03
```

Figure 22 Representation of the 3D matrix

The matrix shown is taken from one of the cases produced during this work. Here and in the following, the considered geometry is to be intended as a small rectangle cut in the tokamak wall. The directions X, Y, and Z should be identified with the toroidal, poloidal, and radial directions, respectively. These 3 directions have been identified with the direction of the toroidal magnetic field, poloidal magnetic field, and the major radius as reported in section 1.

The results in figure 22 should start from the radial position Z= -4 cm (as written in the top part of the figure), but since there is no energy deposition in vacuum and the geometry starts at Z= 0 cm, the values of the energy are zero until the beginning of the geometry. This can be observed from the first lines under "accurate deposition along the track requested". Once the solid wall is reached, the energy deposited in each bin is reported and each value in the file corresponds to a unique position in the Cartesian binning mesh. The results are shown in such a way that first there is an iteration over the X index, then the Y index, and finally the Z index. In this specific case, it means that the first value of the matrix corresponds to the position A(1,1,1) then there is an iteration on the X index which goes as A(2,1,1) A(3,1,1) until A(NX,1,1). Once the iteration over X is completed, the Z index is increased by one since in this specific case the number of bins along Y is equal to 1. The iteration would be in the form A(1,1,2) A(2,1,2) A(3,1,2) until A(NX, 1,2) and so on with the final position equal to A(NX,NY,NZ).

In order to represent the energy deposition plots, FLUKA automatically merges the file containing the 3D matrix. The user can choose if the data need to be represented as a 2D projection or 1D projection through the interface shown in figure 23.

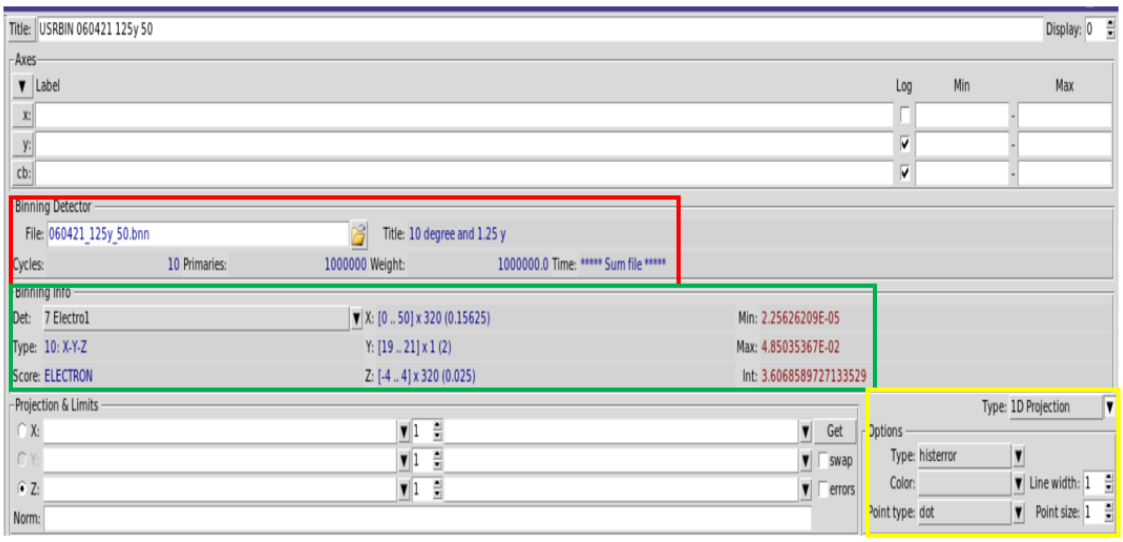

Figure 23 FLAIR interface for the representation of the results: Output file selection (red box), type of detector (green box), type of visualization (yellow box)

In the interface shown in figure 23, the user can select (in the red box) the output file to plot. If different detectors are used, also the detector has to be selected in the green box and the type of visualization in the yellow box. The detectors are the estimators activated on the geometry defined by the users and can trace the particle fluence, the energy deposition, or any other desired output. The types of visualization are, mainly, the 2D projection or the 1D projection of the results. The plots produced by this process in this work are shown in subsection 7.3.

One of the advantages of the FLAIR interface is that it allows extracting any result file which has to be first converted into an ASCI text file to be readable. The extracted files can then be further analyzed in external software like MATLAB in order to produce any further desired analysis. For example, this has been done to compare the results obtained in this work and the ones obtained by the ENEA case study.

6.3. Source of errors

The file reporting the 3D matrix containing the values of the energy deposition, contains also a 3D matrix that shows the percentage errors corresponding to each energy deposition value. In particular, the results given by the code are affected by two types of errors:

- Statistical uncertainties
- Systematic uncertainties

Regarding the statistical uncertainties, these depend on the number of particles and cycles simulated. It has been observed that if an estimator receives enough contributions n, the statistical error uncertainty of the estimator goes as $1/\sqrt{n}$ with the number of simulated particles (FLUKA, 2020).

The variance of a scored observable X, which in this study is the energy deposition, is given by the expression (13).

$$\sigma^2_{<x>} = \frac{1}{N-1}\left[\frac{\sum_1^N n_i x_i^2}{n} - \left(\frac{\sum_1^N n_i x_i}{n}\right)^2\right] \quad (13)$$

where,

N is the number of cycles in which the total number of particles are grouped

n_i is the number of simulated particles per cycle

n is the total number of primaries

x_i is the average of the i-th cycle: $x_i = \sum_{j=1}^{n_i} \frac{x_{ij}}{n_i}$

In order to have a reasonable statistical error, the FLUKA experts recommend simulating a number of cycles around 5-10 with a high number of particles. That is, the error bars reduce by $1/\sqrt{n}$ (FLUKA, 2020). In addition, if only one cycle is

run, expression (13) could not be evaluated since the first factor of the product would give 1/0 and FLUKA will return an uncertainty of 100%.

Regarding the systematic errors, these depend on multiple factors, among which:

- Implemented physical models
- Inaccurate material composition
- Cross-section data uncertainty
- Beam losses
- Simplification of the geometries
- Bugs present in the software
- Various user mistakes

All these sources of systematic errors can influence the result and are not easily addressable.

FLUKA allows the user to define a specific estimator with an external routine that can be plugged in the code, however, for this study this option has not been utilized. At the same time, the user routine for the source definition has been used to define sources in accordance with the experimentally observed REs energy distributions for some shots in JET.

6.4. User routines

The in-build sources present in the FLAIR interface are:

- A monoenergetic beam, as the one used to analyze the impact of REs on the EU-DEMO FW
- A beam with a Gaussian energy distribution with respect to a mean value

In order to build experimentally observed beams, user routines have to be used. These routines replace part of the FLUKA code shown in the FLAIR interface and are written in Fortran 77. They are already present in the FLUKA database as it is shown in figure 24, and they have to be extracted in order to be modified and compiled in the code environment using the build option.

The sources can be built in multiple ways, for this study the energy distribution has been implemented through a polynomial expression which represents the weight function. For further details see section 8.

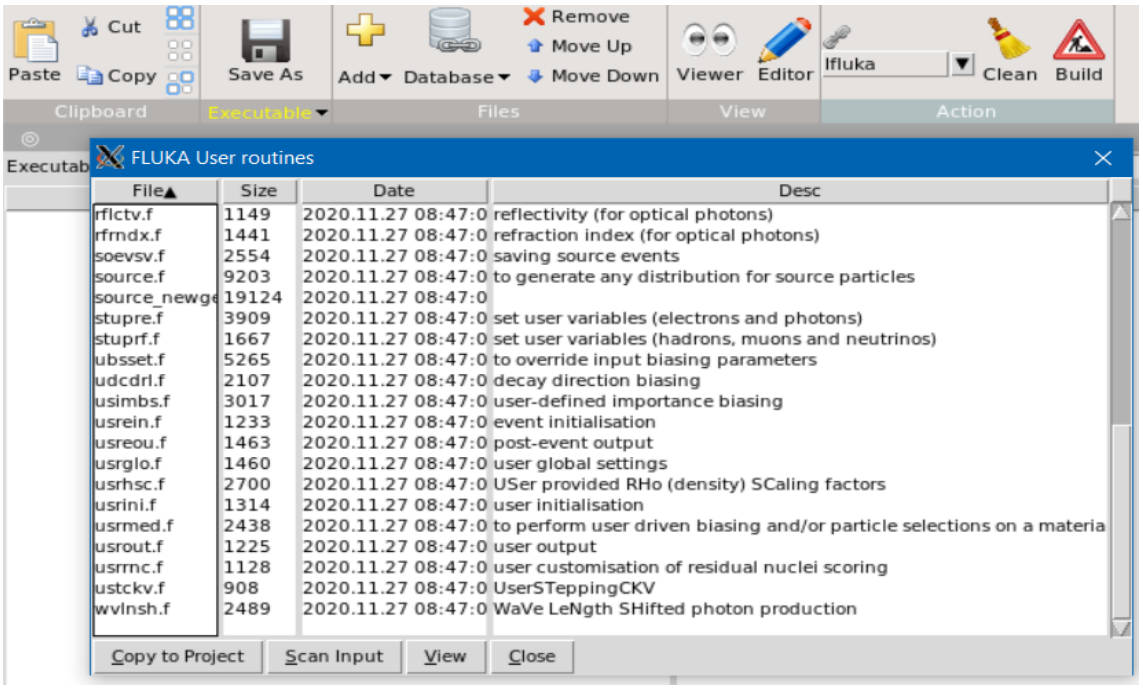

Figure 24 Interface for the user routine selection

Once the user routine is ready, it can be compiled in FLAIR and the electron spectrum can be verified. This is done by using a built-in estimator called USRBDX which estimates the fluence of particles as a function of their energy. This is usually done in FLUKA by placing a sphere around the source location and scoring the number of particles exiting from the sphere to the outside region. The sphere is made of vacuum, so it does not influence the estimated spectrum.

The procedure adopted for implementing the REs beams measured in FLUKA and the results obtained are presented in section 8.

7. Runaway Electron Impact on EU-DEMO First Wall

The study of Runaway generation and interaction with the PFCs will become even more critical in future reactors. Until now, the first wall of the reactors was the wall of the vacuum chamber and ITER is going to have a FW (that will be different from the wall of the vacuum chamber). However, it will be not followed by the breeding blanket, which instead will be the case of DEMO. In DEMO, the FW will be the plasma-facing surface of the breeding blanket (BB) and it will protect the BB itself from plasma exposure. Nevertheless, the FW will be a thin structure (approximately 3 cm) and since the runaway electrons can deposit their power in very localized spots, they may damage the breeding blanket, the cooling tubes causing leakages, etc.

For this thesis, a study of the energy deposition in EU-DEMO FW due to REs has been carried out using FLUKA. This has been possible thanks to a partial availability of input parameters taken from a case study done by ENEA in the framework of EUROfusion Workpackage WPMI (Federici, 2019). In the following subsections, the FW geometry implemented for the study is described. In the last two subsections, the work is presented, and the results are discussed along with a comparison with the results of the ENEA case study.

7.1. EU-DEMO First Wall

The DEMO reactor is going to have a component that is not present in the current fusion machines and will not be present in ITER. This is the breeding blanket that will be used for:

- Production of tritium for reactor tritium self-sufficiency
- Power extraction to produce electricity

These two functions lead the materials to work in a high neutron environment since the neutrons produced through fusion reactions will be used for both the underlined purposes. Moreover, additional constraints are imposed for the structure as now the aim is not only to limit the damage to the PFCs but to have a structure that allows enough high energy neutrons to pass through it in order to produce tritium and extract power through neutron slowing down. As a consequence, the FW of the DEMO reactors is a relatively thin structure (~ 3 cm) and the heat loads that it can handle are relatively moderate, strengthening the need for systems able to mitigate the plasma events that could damage it. In figure 25, a schematic representation of the first layers of the blanket structure is given.

As it can be noticed in figure 25, Be is not used anymore and two different materials are used. Tungsten is the armor material, due to its good

thermomechanical properties, while Eurofer fills most of the rest. Eurofer was chosen because of its high tolerance to neutron irradiation. In order to have an efficient power conversion, helium or water at high pressure is used as coolant.

For this study, the water-cooled configuration has been used, to be in line with the configuration adopted by ENEA. The first wall geometry is subdivided into 36 modules, with each module having the dimensions shown in figure 26 for the tungsten thickness and the size of the coolant channels; the cooling channels are assumed to be along the poloidal direction (Federici, 2019).

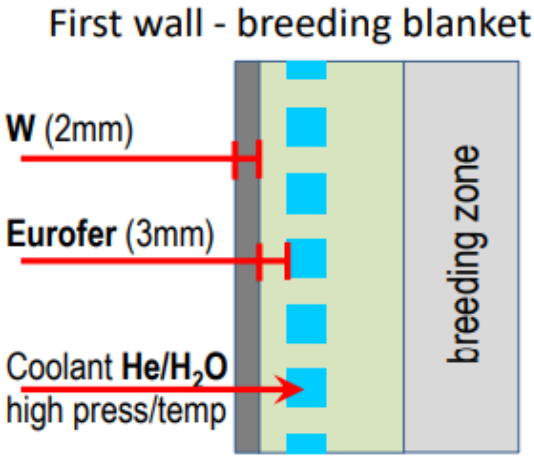

Figure 25 Schematic representation of the first layers of the blanket structure with the used materials (Siccinio, 2020)

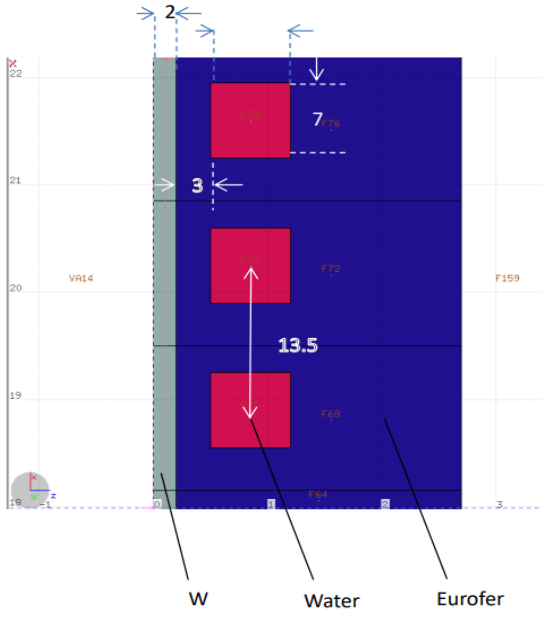

Figure 26 First wall composition with dimensions in mm (Federici, 2019) : tungsten (grey – 2 mm), Eurofer (blue - 3 mm between tungsten and coolant channels) and Coolant channels (red – squared channels of 7 mm side)

7.2. Description of Work

For the simulations regarding the EU-DEMO FW, an already available beam of electrons has been used which does not require defining any user routine. The geometrical model consists of a 3-D layered structure with the X-, Y- and Z-axis oriented along the toroidal, the poloidal, and the radial direction, respectively. In addition, uniform conditions are assumed for the poloidal direction, in order to produce the energy deposition in the Z-X geometrical plane.

The work consisted in irradiating a geometric sample of EU-DEMO first wall with a monoenergetic electron beam having an energy of 20 MeV. Two different beams have been implemented:

- A beam with an incidence angle of 1 degree with respect to the toroidal direction, as shown in figure 27. In figure, the solid wall is zoomed in order to show the beam direction. For simplification purposes, this beam will be called Beam1 in the following

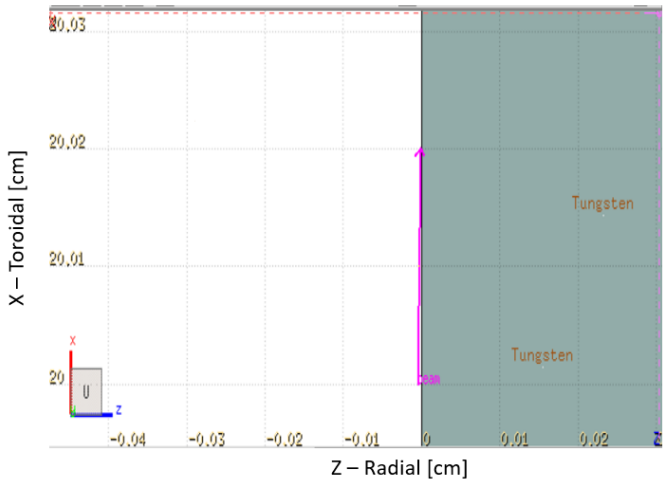

Figure 27 REs beam hitting the FW with Beam1

- A beam with an incidence angle of 10 degrees with respect to the toroidal direction, as shown in figure 28. For simplification purposes, this beam will be called Beam2 in the following

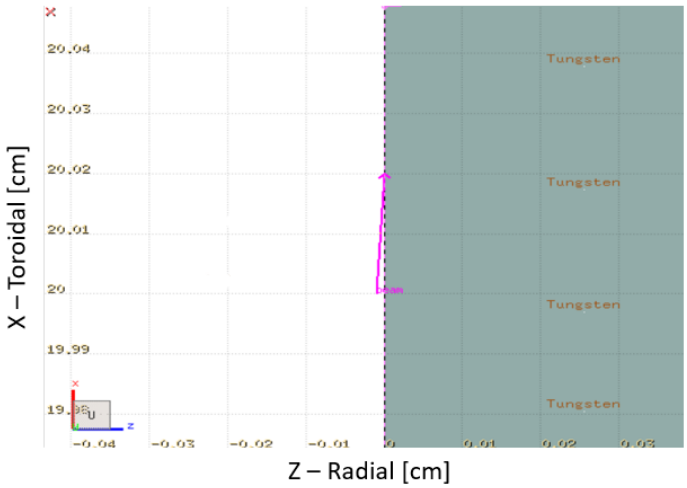

Figure 28 REs beam hitting the FW with Beam2

The dimensions of the beam hitting the wall are the same for the two beams along the toroidal direction while they are different along the poloidal direction. This is done to reproduce the curves that have been obtained from the case study of ENEA where the beam dimensions are not specified along the poloidal direction. Along X, the electron beam has a length of 50 cm as the sample total toroidal length and along y it is 0.15 cm for Beam1 and 1.25 cm for Beam2. In both cases, the beams hit the wall at X=20 cm, Y=20 cm, and Z=0 cm.

Once the beam characteristics are defined, the next step regards the geometry of the wall which is the same as in figure 26 with a toroidal extension of 50 cm, a poloidal extension of 2 cm, and a radial extension of 2.7 cm in line with the dimensions taken by ENEA (Federici, 2019). A 2D and 3D representation of the geometry is shown in Figures 29a and 29b, respectively. The figures have been taken from the geometry tab of the FLAIR interface.

Regarding the geometry definition in FLUKA, the code requires defining the geometry going from outside to the core. That is, first the surrounding regions have to be defined which are pre-defined in FLUKA and are called blackbody which represents the region to which the fraction of the beam energy not deposited in the sample is lost and a vacuum region to separate the blackbody from the geometry. For this study, an additional vacuum region has been defined to have a visualization of the plots produced by FLAIR. Once the vacuum region is defined, the geometry can be implemented starting from a block of Eurofer and then adding tungsten as the first layer and the coolant channels.

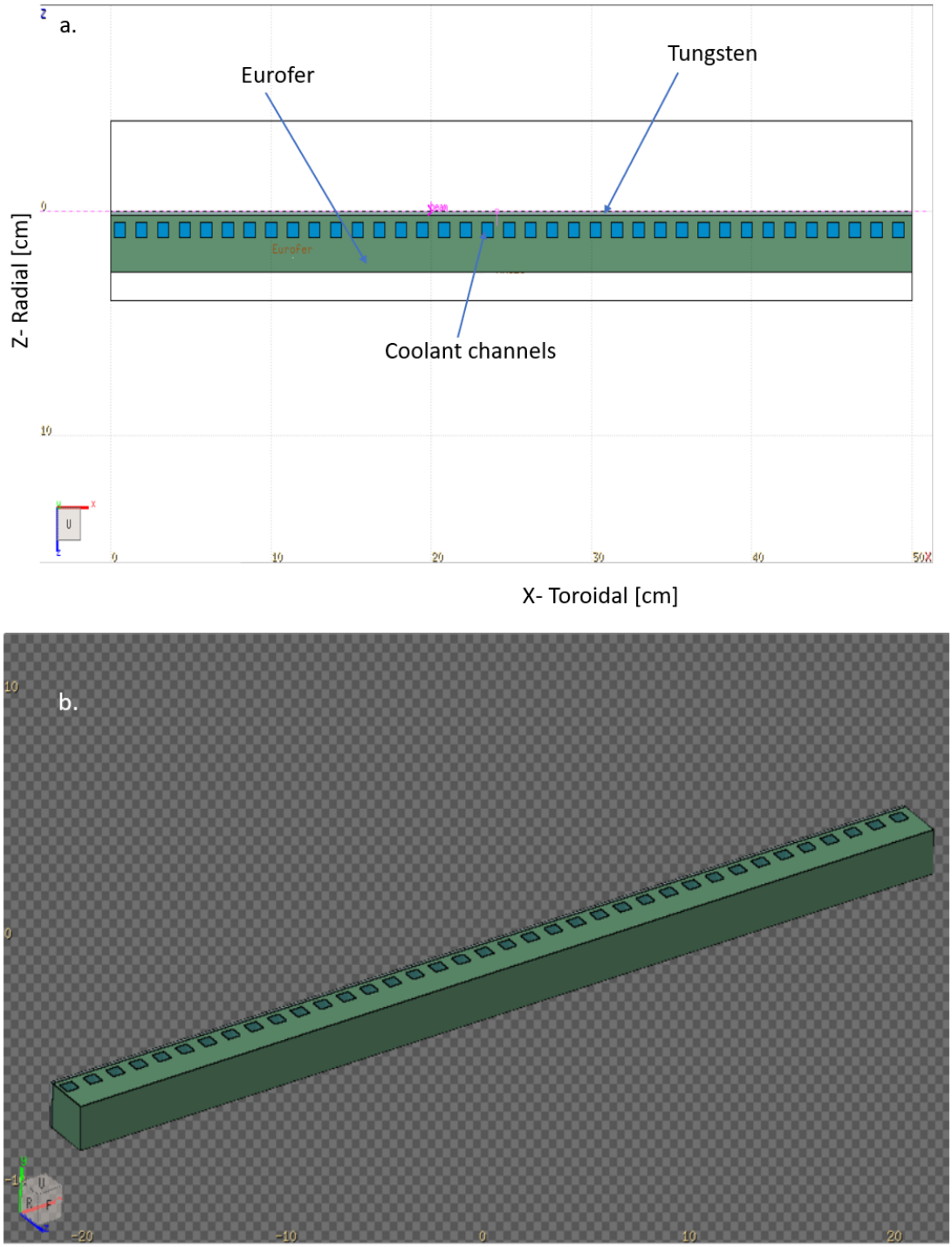

Figure 29 Representation of the geometry sample with a beam incidence angle of 10 degrees: a) 2D representation: : Tungsten (grey), Eurofer (green) and coolant channels (blue), b) 3D representation

Regarding the material composition of the sample tungsten and water are already present in the material database of FLUKA while Eurofer has to be defined by the user since it is not given. The Eurofer composition that has been used for this study is reported in Table 1 (Paú et al., 2006). This composition could

be different from the one used by the authors of the ENEA case study since it is not described in their report.

Table 1 Eurofer-97 chemical composition (Paú et al., 2006)

Element	%	Element	%
Fe	88.63	W	1.08
Al	0.11	Cu	0.05
Si	0.16	C	0.11
V	0.21	S	3.5e-4
Cr	8.86	H	1.12e-4
Mn	0.47	Ca	8.0e-5
Ta	0.32		

The dimensions of the estimator (called Estimator1 in the following) covering the whole geometry are 0<X<50 cm, 19.975<Y<20.025 cm, and -4<Z<4 cm, and the estimator dimensions are subdivided in bins:

- 250 bins along the toroidal direction with each bin having a length of 0.2 cm
- 1 bin along the poloidal direction
- 40 bins along the radial direction with each bin having a length of 0.2 cm

The beam irradiates the whole sample, however, the deposited energy is traced on a small fraction of the entire geometry as well. The dimensions of this fraction are 16<X<24 cm, 19.975<Y<20.025 cm, and -4<Z<4 cm and the estimator dimensions (called Estimator2 in the following) are subdivided into bins for a good resolution of the results:

- 320 bins along the toroidal direction with each bin having a length of 0.025 cm
- 1 bin along the poloidal direction
- 320 bins along the radial direction with each bin having a length of 0.025 cm

The part of the geometry to which the Estimator2 is applied is shown in figure 30.

The dimensions of the estimators and the number of bins for both estimators have been taken from the ENEA case study in order to make a comparison with the results of the case study. However, for the case of Estimator1, NX=320 and NZ=320 has been used as well (called Estimator1 modified in the following) to shows the improvement in the resolution of the results.

The last input to define in order to carry out the simulation is the number of test particles and the number of cycles. In order to attain reasonable statistics, 100k test particles are simulated for 10 cycles; the results will be shown in the next subsection.

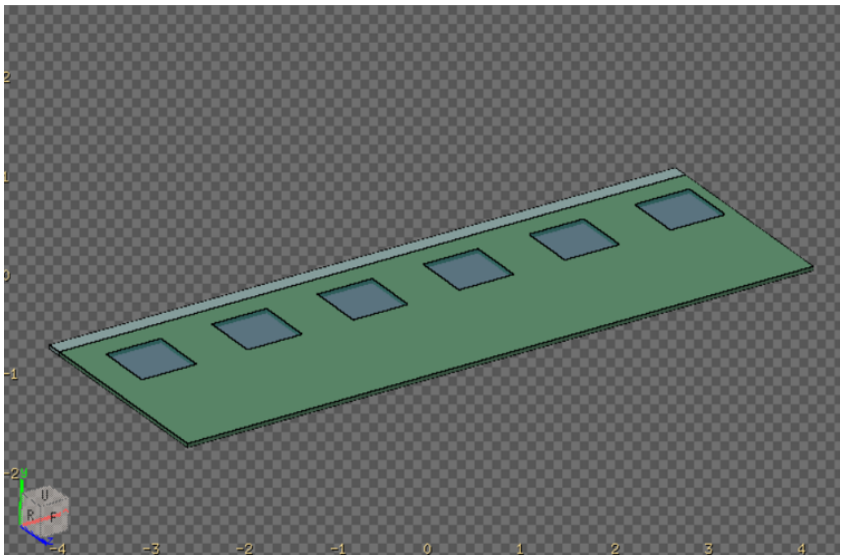

Figure 30 3D Representation of the geometry over which the energy deposition is traced

7.3. Results

As reported above, two different incidence angles have been analyzed and a comparison is made with the results obtained by a previous study performed by ENEA. The following subsections present the results for the Beam1 and Beam2 with USRBIN estimator activated on the entire sample (Estimator1), on a fraction of the sample (Estimator2), and a comparison with the results obtained in the ENEA case study.

7.3.1. Results with estimator covering the whole geometry

In this case, the deposited energy is traced throughout the entire sample of the geometry. In table 2, the energy deposition in the main regions of the geometry is shown for Beam1 while in table 3 for Beam2. The region named “Blackbody”

is the second region surrounding the geometry studied by the user and it represents the region to which the particles of a species are lost after escaping from the system. In figure 31, the two surrounding regions are shown.

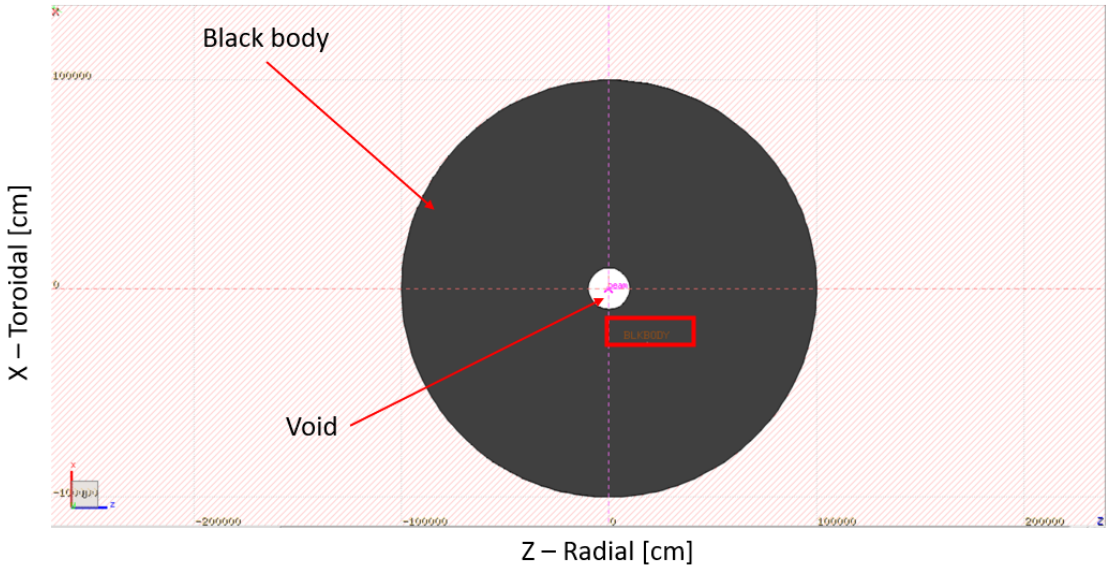

Figure 31 2D representation of the black region (black circumference), void region (white circumference), and the wall identified by the beam position

In figure 31 the void region is a circumference of 10000 cm radius while the black region is a circumference of 100000 cm radius, and these dimensions are given as default by the code.

On the other hand, the region Tungsten Eurofer and coolant channels correspond to the different geometry components as shown in figure 29a.

Table 2 Amount of energy deposited in each region of the sample with Beam1

Region	Energy density [MeV/cm^3 per electron]
Blackbody	13.59
Void	0
Eurofer	0.94
Tungsten	5.43
Coolant channels	0.04

Table 3 Amount of energy deposited in each region of the sample with Beam2

Region	Energy density [MeV/cm^3 per electron]
Blackbody	9.47
Void	0
Eurofer	2.70
Tungsten	7.65
Coolant channels	0.18

Tables 2 and 3, contain the energy deposited in each region and different values are obtained for two different incidence angles. In particular, with a lower incidence angle, the fraction of energy lost to the black body is higher. Indeed, with Beam1 13.59 MeV are lost to the surrounding region compared to 9.47 MeV with Beam2. This is because with an incidence angle of 1 degree the electrons have to travel a distance that is 10 times greater than the distance traveled by the electrons with an incidence angle of 10 degrees to reach a certain radial depth. As a consequence, the probability of an electron escaping from the system because of the interactions with the matter is higher. To demonstrate this reasoning, in figure 32 the comparison between the electron fluences observed in the wall with Beam1 and Beam2, respectively, are shown. In the figure, the fluence along the radial direction is shown using the USRBIN estimator activated on the entire sample. However, instead of the energy, the electron fluence is traced. The fluence expresses the number of particles crossing a certain area and in FLUKA the fluence is computed through the ratio between the path traveled by the particle inside a bin and the volume of the bin (FLUKA, 2020).

In figure 32, it can be observed that, although, the electron fluence is similar at Z=0 cm (~5e-2 cm^{-2}), as the radial position increases the difference between the two curves becomes more evident. This is because a larger number of particles escape from the domain when the incidence angle is equal to 1 degree.

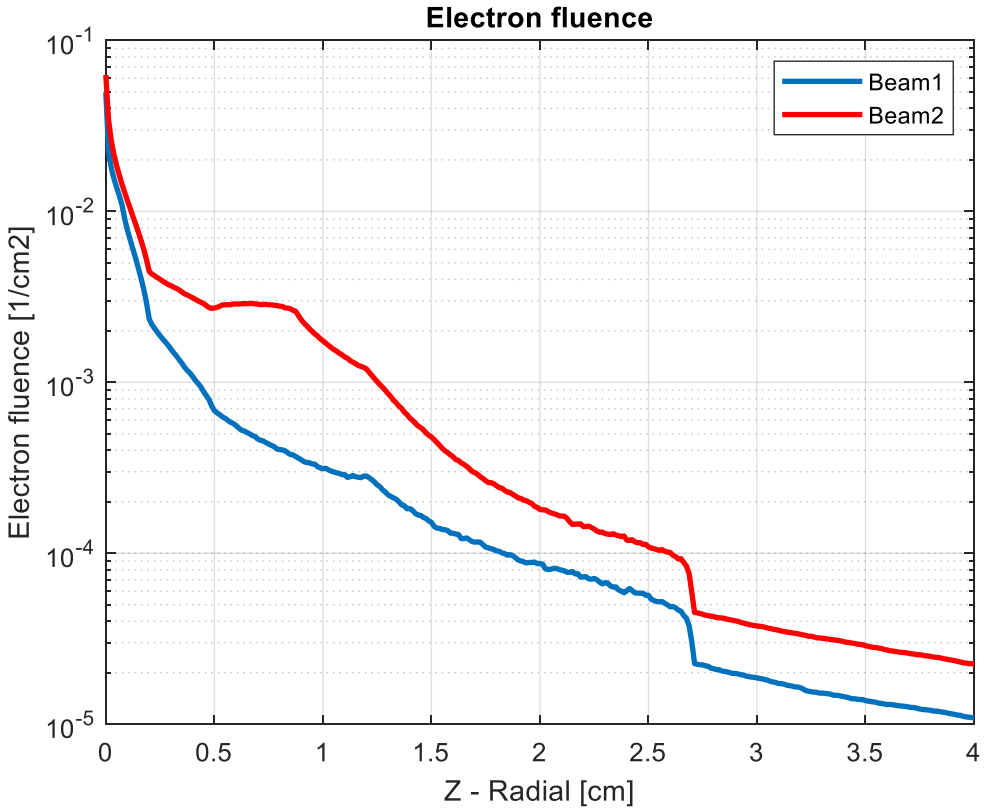

Figure 32 Comparison between the electron fluence given by USRBIN estimator with Beam1 (blue) and Beam2 (red)

The poloidal extension of the two beams differs as well, however, as it can be seen in table 4, the influence of the poloidal extension of the final deposition energy is not as significant as the influence of the incidence angle. Indeed, the difference in the energy lost to the surrounding region between a beam of poloidal extension 0.15 cm and 1.25 cm is around 0.01 MeV, both having an incidence angle of 1 degree. On the other hand, the difference in deposited energy between Beam1 and Beam2 is around 4.12 MeV.

A second observation that can be made about the results shown in tables 2 and 3 is related to the amount of energy deposited in tungsten. The total deposited energy with Beam1 is around 6.4 MeV and 10.54 MeV with Beam2. The tungsten layer takes up around 85% of the total deposited energy with Beam1 and 74% with Beam2. This demonstrates the capability of tungsten to protect the structural material behind it. However, this could lead to damage in tungsten as shown in figure 7.

Table 4 Energy deposited in each region with a beam of 1 degree incidence angle and a poloidal extension of 1.25 cm

Region	Volume in cubic cm	Energy density [MeV/cm^3 per electron]
Blackbody	1	13.58
Void	1	0
Eurofer	1	0.91
Tungsten	1	5.47
Coolant channels	1	0.04

The difference in the energy deposition in the tungsten layer with Beam1 (85%) with respect to the wall with Beam2 (74%) is related to the same reason that leads to a different deposition of energy in the wall with the two Beams. That is an electron with an incidence angle of 1 degree travels a larger distance in the tungsten layer depositing higher energy with respect to an electron with an incidence angle.

The visualization of the different energy deposition intensity can be observed also in figure 33 and 34 that shows the 2D projection on the ZX geometrical plane of the deposited energy with Beam1 and Beam2, respectively. In addition, an improvement in the resolution of the results can be observed between Figure 33a and 33b and Figure 34a and 34b.

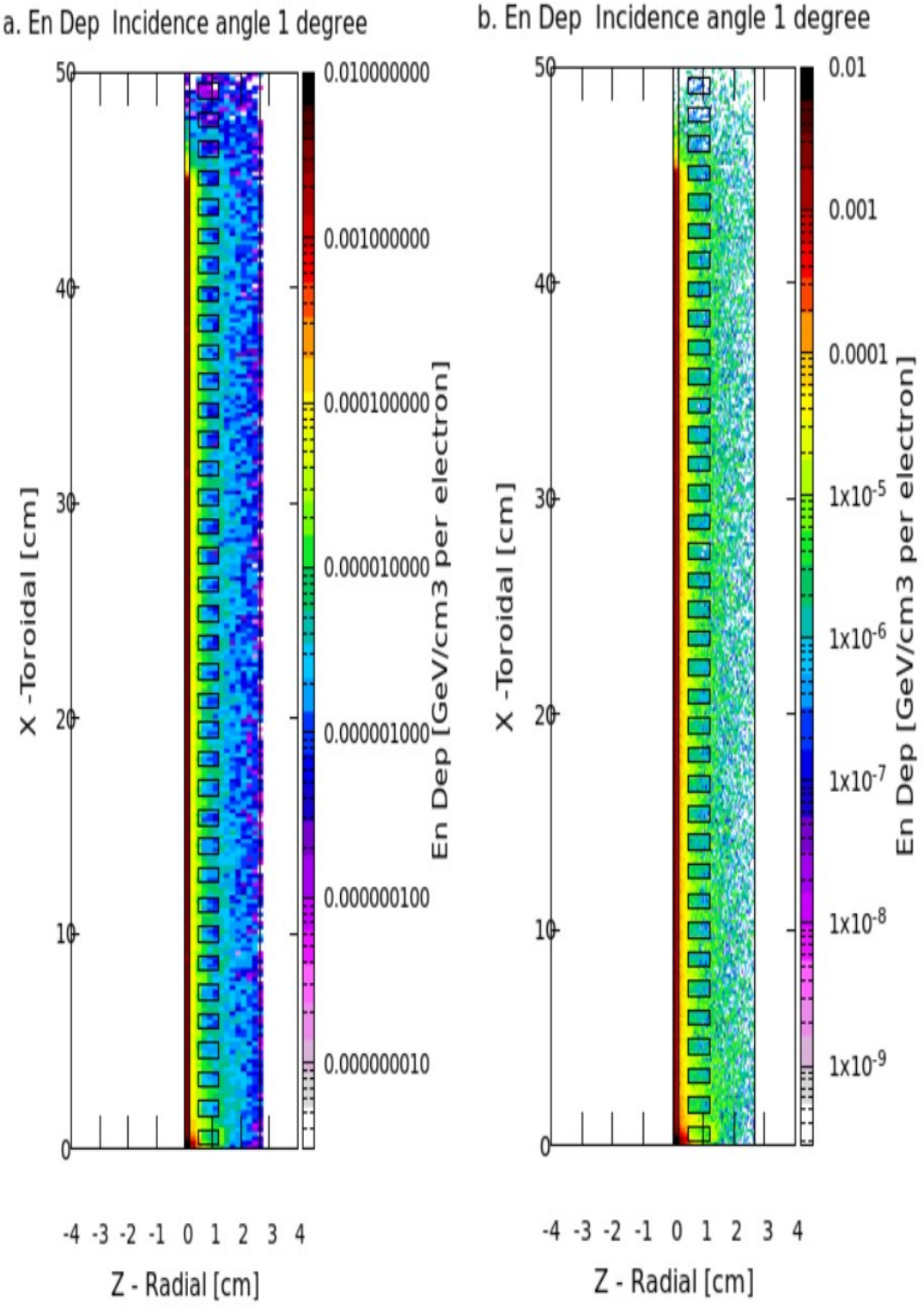

Figure 33 2D projection on the ZX geometrical plane of the energy deposition with Beam1 using a) Estimator1 (low resolution) results b) Estimator1 modified (high resolution)

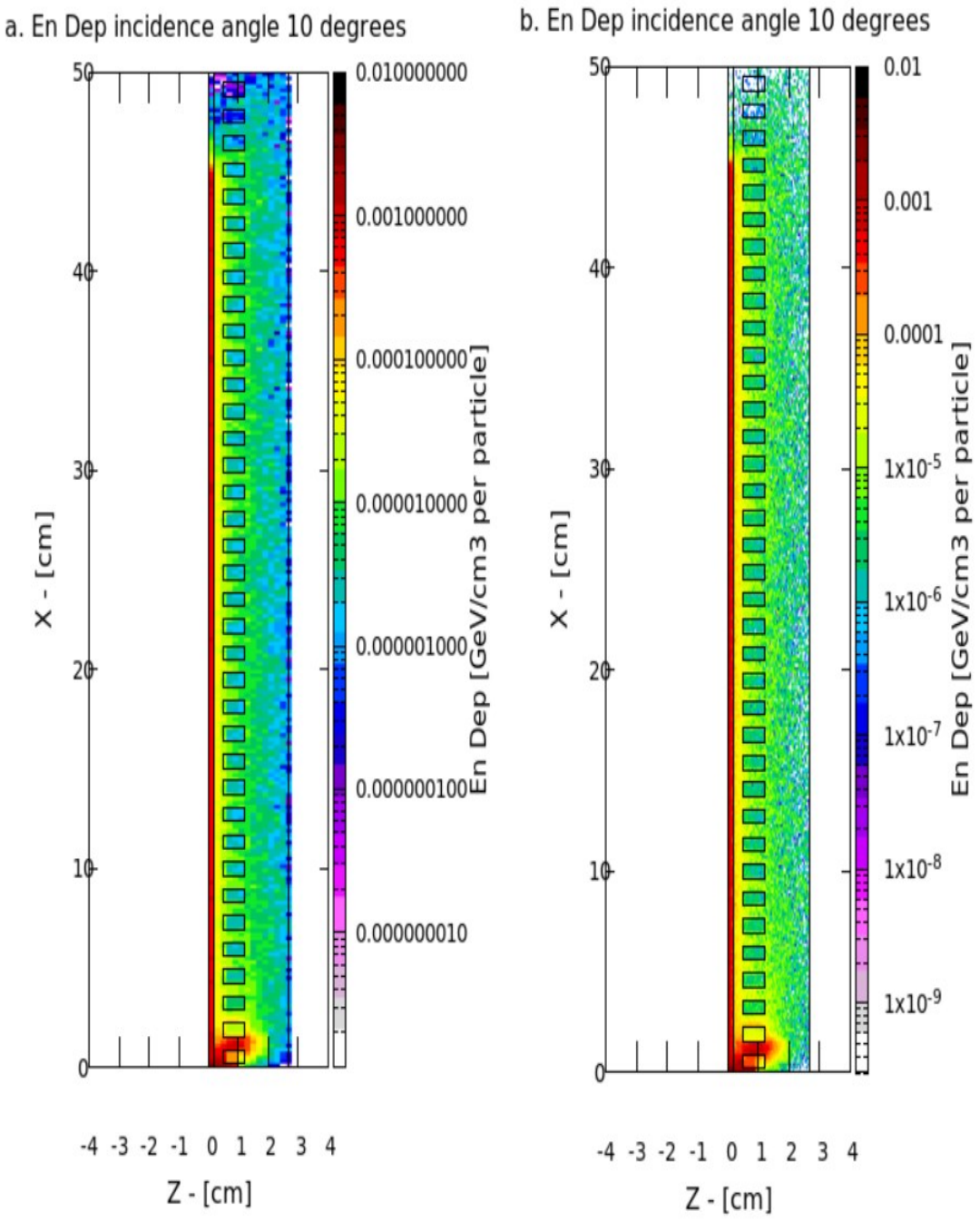

Figure 34 2D projection on the ZX geometrical plane of the energy deposition with Beam2 using a) Estimator1 results b) Estimator1 modified

As it can be observed in figures 33 and 34, the tungsten layer gets the highest deposition of energy. In addition, as underlined above Beam1 leads to a lower energy deposition with respect to Beam2.

In the central part of the geometry, the energy deposition appears to be uniform in both cases, however, at the boundaries, the energy deposition is not uniform. In particular, in figures 33 and 34, the lower boundary experiences a high energy deposition while the upper boundary experiences a lower energy deposition. The

reason for this behavior is related to the beam toroidal extension and the beam length. The beam hit the sample at X=20 cm and it has a width of 50 cm that means the minimum and maximum value of X for the beam is -5 cm and 45 cm, which does not cover the last fraction of the wall. As a consequence, the energy deposited in this region is lower. On the other hand, the peak in the energy deposition in the lower boundary might be related to the beam hitting the geometry not only in the front but also laterally since the geometry starts at X=0 cm and the beam at X= -5 cm.

7.3.2. Results with estimator covering a fraction of the geometry

In order to get a better visualization of the results and to avoid the non-uniformities that take place at the boundary of the sample, an estimator is applied to the central part of the geometry symmetric to the beam incidence position, that is 16<X<24 (Estimator2). The 2D projection of the deposited energy is shown in figures 35 and 36 with Beam1 and Beam2, respectively.

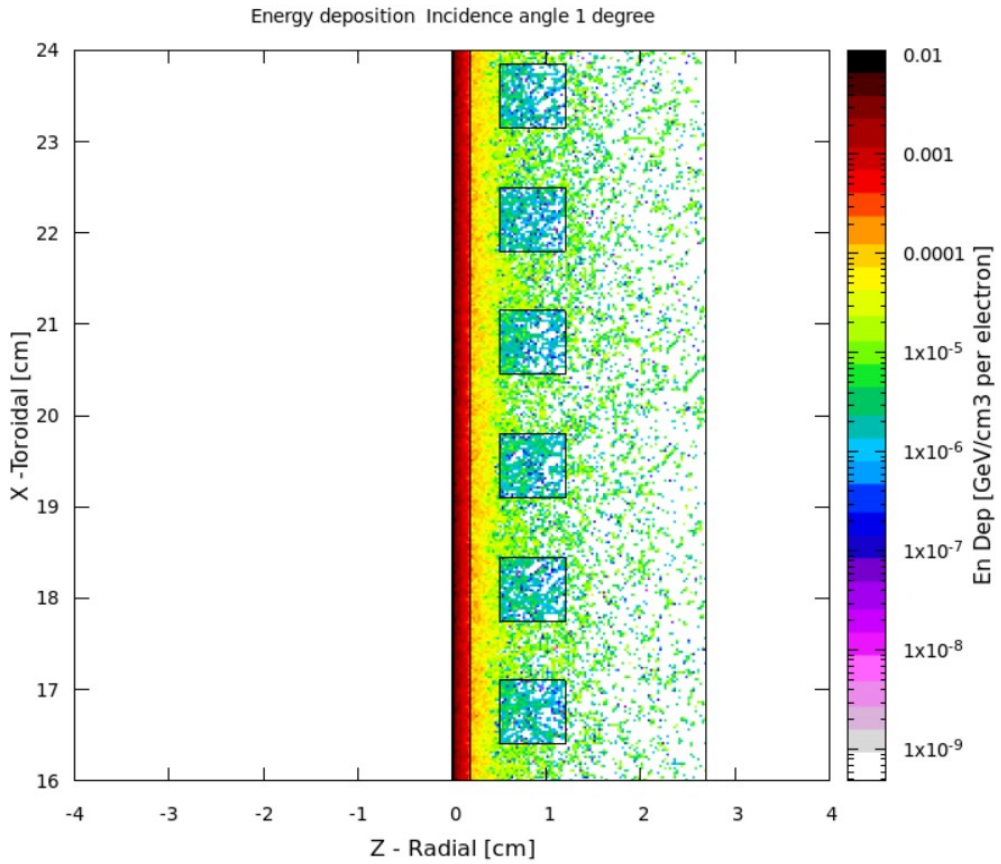

Figure 35 2D projection of the deposited energy on the ZX plane with Beam1 and Estimator2

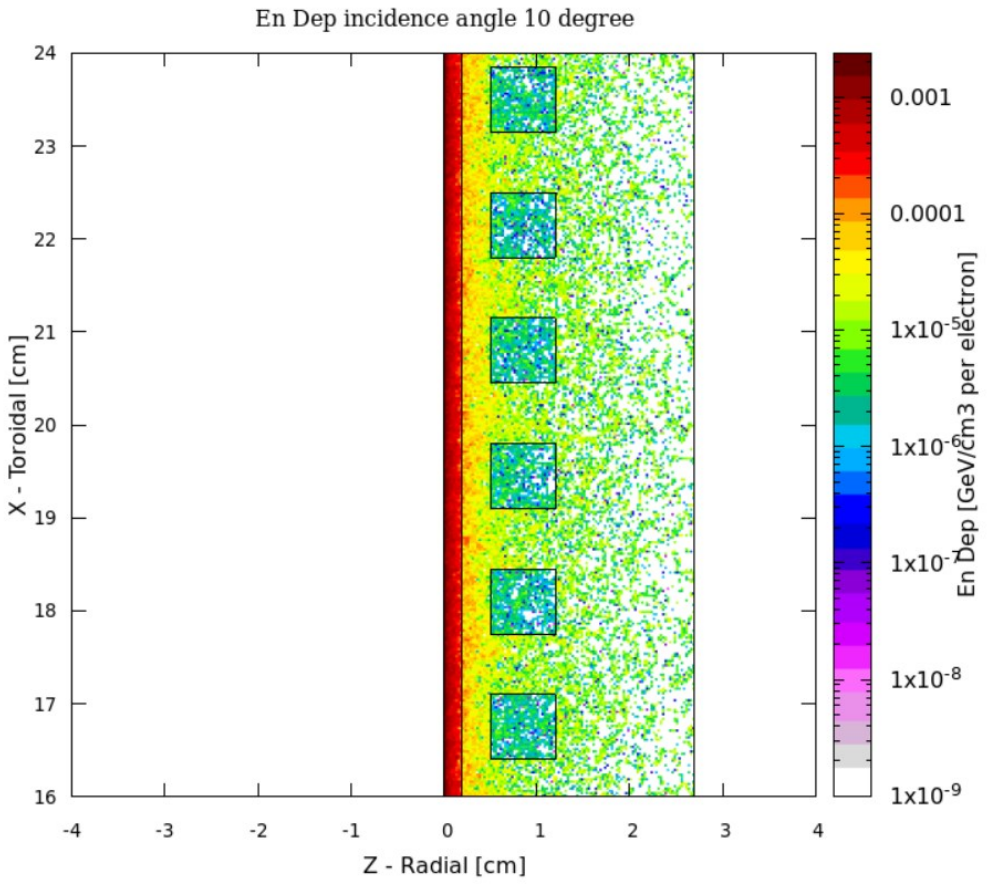

Figure 36 2D projection of the deposited energy on the ZX plane with Beam2 and Estimator2

As it can be observed in figures 35 and 36, the major deposition takes place in the tungsten while towards the end of the geometry along the radial direction the energy deposition is 6 orders of magnitude lower than the initial layer. In addition, the deposition differs in the fraction of the geometry between 0.5<Z<1.2 where the coolant is present.

Even if in figures 33 and 34, it seems that the coolant channels are not squared, in figures 35 and 36 it can be observed that the coolant has a squared form. This is due to the different aspect ratios of the figures showing the entire geometry and a fraction of it.

In figures 37 and 38, the 1D projections of the deposited energy along the radial direction are shown with Beam1 and Beam2, respectively. For better visualization, the different materials have been underlined as well. As it can be observed in the figures, tungsten has the highest stopping power being able to reduce the deposited energy by 2 orders of magnitude, protecting the underneath materials.

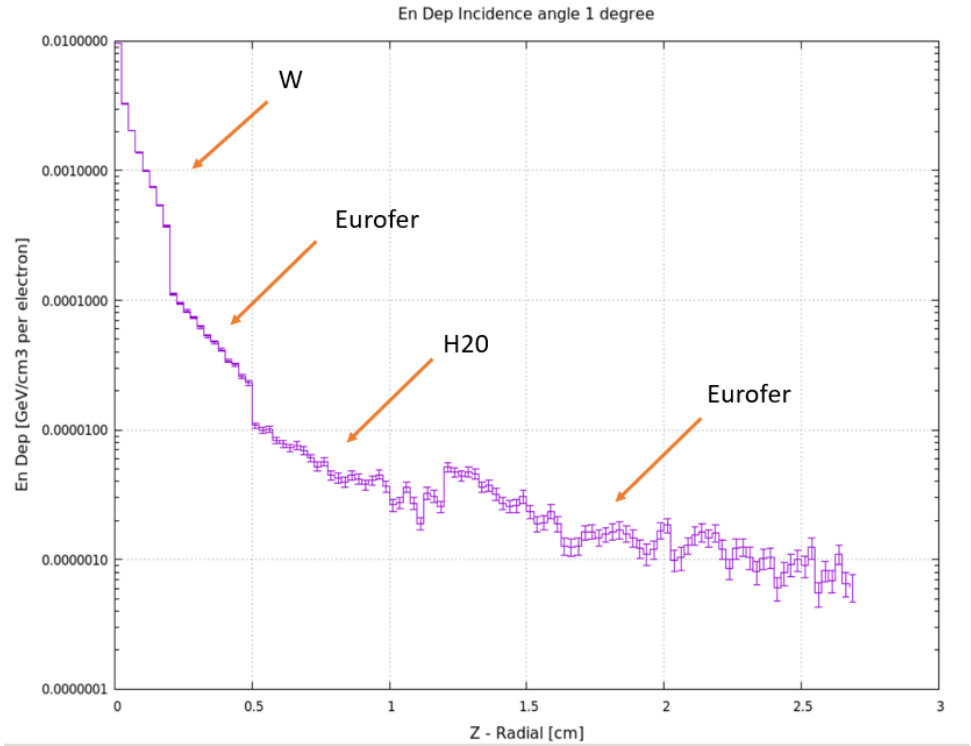

Figure 37 1D projection along the radial direction of the deposited energy with Beam1 and Estimator2

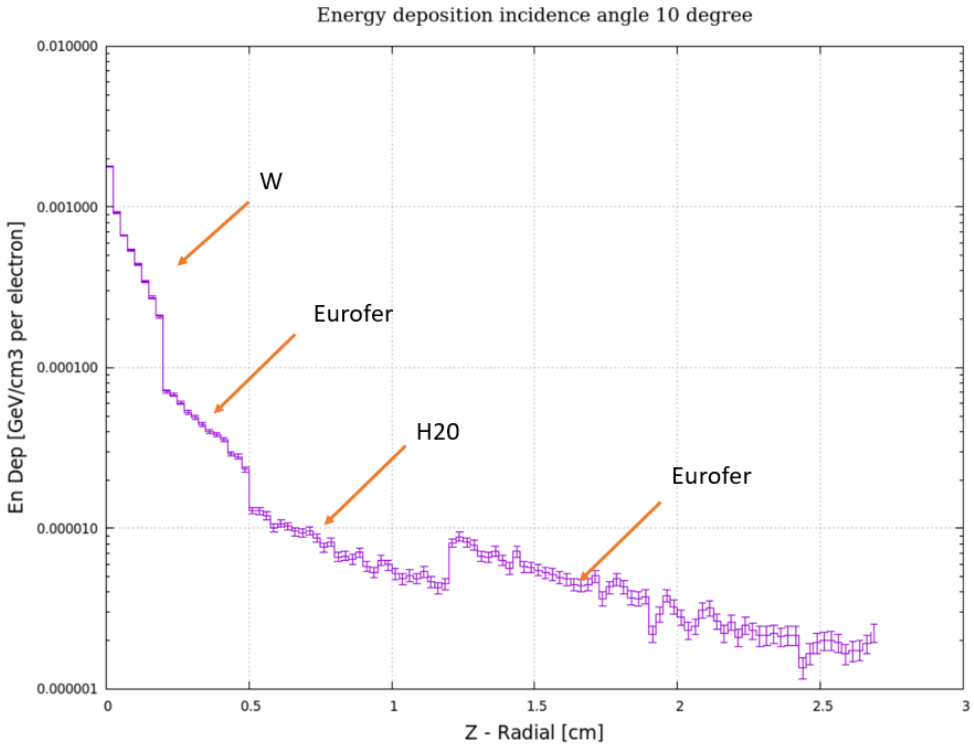

Figure 38 1D projection along the radial direction of the deposited energy with Beam2 and Estimator2

The major difference between figures 37 and 38 is related to the energy reported at the radial position Z= 0 cm being around 0.01 GeV/cm^3 for Beam1 with respect to 0.002 GeV/cm^3 for Beam2. This is mainly due to the different poloidal extension of the electron beams since the beam is 0.15 cm along Y in Beam1 and 1.25 cm in Beam2. Since, the estimator has a poloidal length of 0.05 cm (19.975<Y<20.025 cm) and the beam hit the surface at Y=20 cm, when the beam extension is 0.15 cm in the Y direction, initially, a large fraction of the deposited energy is detected by the estimator while in the case of Beam2 the energy is distributed on a larger surface and only a part of is detected by the Estimator2. To verify this, Beam1 is modified making the poloidal extension equal to 1.25 cm as in Beam2 and the result is shown in figure 39.

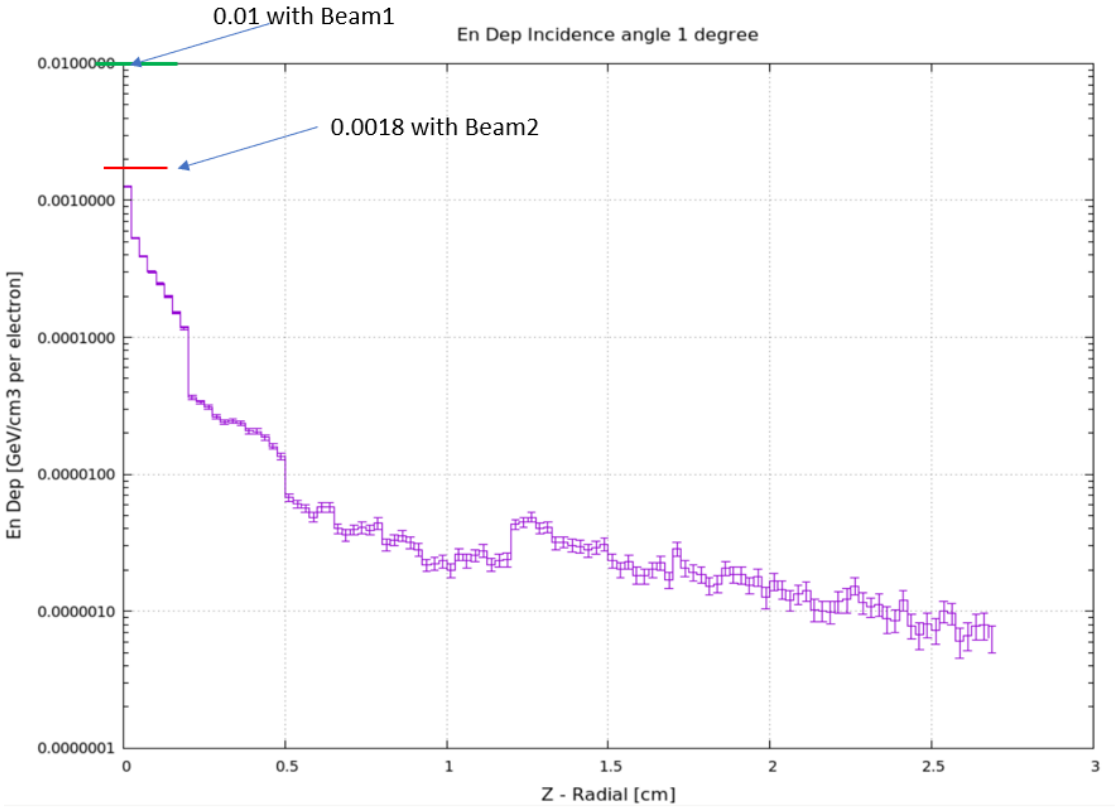

Figure 39 1D projection along the radial direction of the deposited energy with Beam1 having poloidal length 1.25 cm and Estimator2

As it can be observed in figure 39, with a 1.25 cm poloidal length, Beam1 gives a value of the energy around 0.0015 GeV/cm^3 per electron at Z= 0 cm similar to 0.0018 GeV/cm^3 per electron obtained with Beam2 at Z= 0 cm. However, a poloidal extension of 0.15 cm is selected for Beam1 based on the comparison done with the ENEA case study in subsection 7.3.3.

A second observation is related to the error bar shown in the same figures. As the energy reduces, the error gets higher, and this could be explained by the number of particles that can reach the regions underneath. As it can be expected, the electron fluence reduces along the radial direction in both cases, consequently, a lower number of particles leads to higher error bars.

Finally, in figures 40 and 41, the 1D projection of the energy depositions along a radial path not crossing a coolant channel and a radial path crossing a coolant channel are shown, respectively. Both curves have been obtained using Beam2 and Estimator2 reducing the area of interest to a path not crossing the coolant channel (figure 40) or crossing a coolant channel (figure 41).

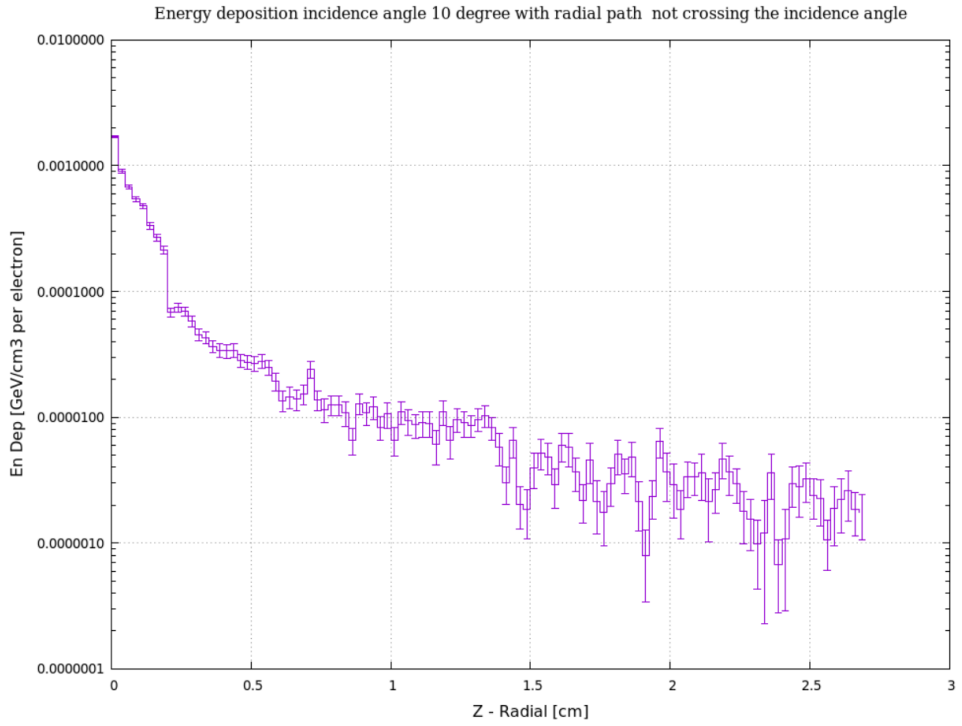

Figure 40 1D projection of the deposited energy along a radial path not crossing a coolant channel with Beam2

With respect to figure 40, in figure 41 the presence of the coolant channel can be observed by the instant reduction in the deposition curve due to a lower stopping power of the water. This can be observed also in table 2 where the energy deposited in the water by the runaway electrons is minimal with respect to the other regions.

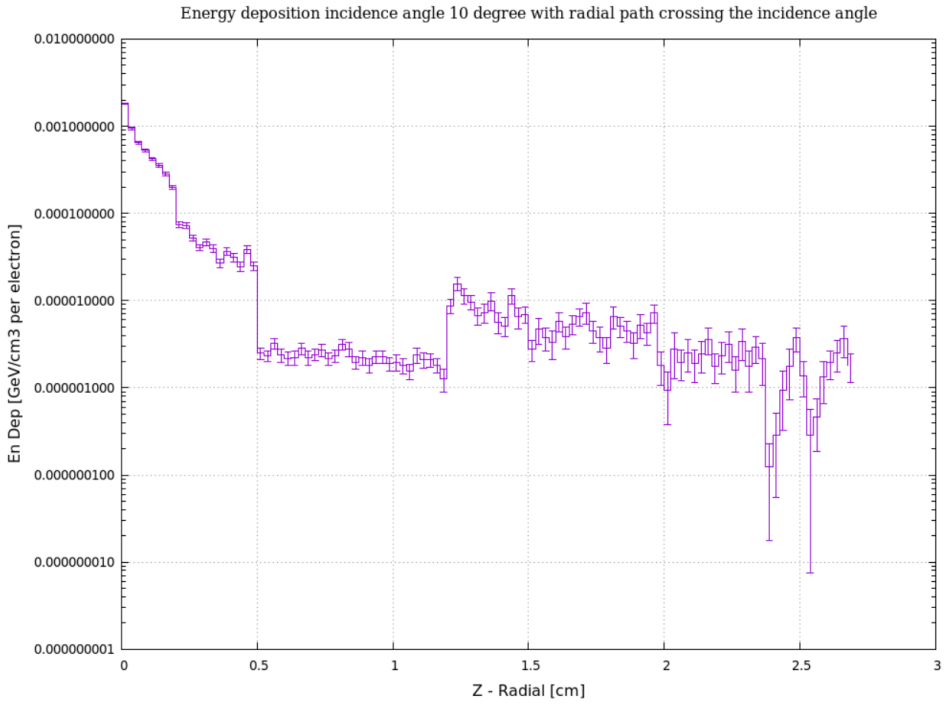

Figure 41 1D projection of the deposited energy along a radial path crossing a coolant channel with Beam2

7.3.3. Comparison of the results with the results of the ENEA case study

As underlined in the previous subsections, the poloidal extension of Beam1 and Beam2 is not given, so a comparison of the results was necessary in order to obtain this value.

From the case study carried out by ENEA, some 3D matrixes necessary to plot the 1D projection of the deposited energy were given. In particular, for Estimator2, results are available for both beams, instead for Estimator1 only the results for Beam1 are available.

From the simulations done in the FLUKA environment, the resulting 3D matrixes were extracted in order to plot the 1D projection in MATLAB. These matrixes were obtained from simulations conducted assuming several poloidal extensions for the two beams.

The 1D projections were obtained by taking the average of the energy deposition over the X direction at a certain radial position. That is if the radial position Z=0 cm is considered, to compute the value of the deposited energy, the average over the toroidal positions at Z=0 cm was taken. This has enabled to obtain qualitatively similar projections to those obtained in FLUKA.

In figure 42, the energy deposition curves for Beam1 with different poloidal widths are compared with the energy deposition curve of the case study. In

particular, y=2 cm, y=1 cm, y=0.5 cm, y=0.25 cm, y=0.15 cm, y=0.1, y=0.05 cm poloidal widths have been used. It can be seen in the figure that as the poloidal extension of the Beam1 reduces, the curve peak at Z=0 cm tends to higher values. The explanation of this behavior has been already explained in subsection 7.3.2. and is mainly due to a reduction in the surface over which the energy is distributed at the starting position. Since the Estimator2 dimensions do not change and the poloidal width of the Beam1 reduces more energy is deposited on the area on which the estimator is present.

In figure 42, it can be observed that Beam1 with y=0.15 cm has the initial part of the energy curve overlapped on the curve reported by the case study. In order to visualize it better, in figure 43, the selected Beam1 is shown in comparison with the curve of the case study. In the figure, it can be seen that the initial parts of the two energy curves are overlapped and this region corresponds to tungsten. However, after the tungsten region, the two curves start to differ with the Beam1 giving lower values for the energy with respect to the second curve.

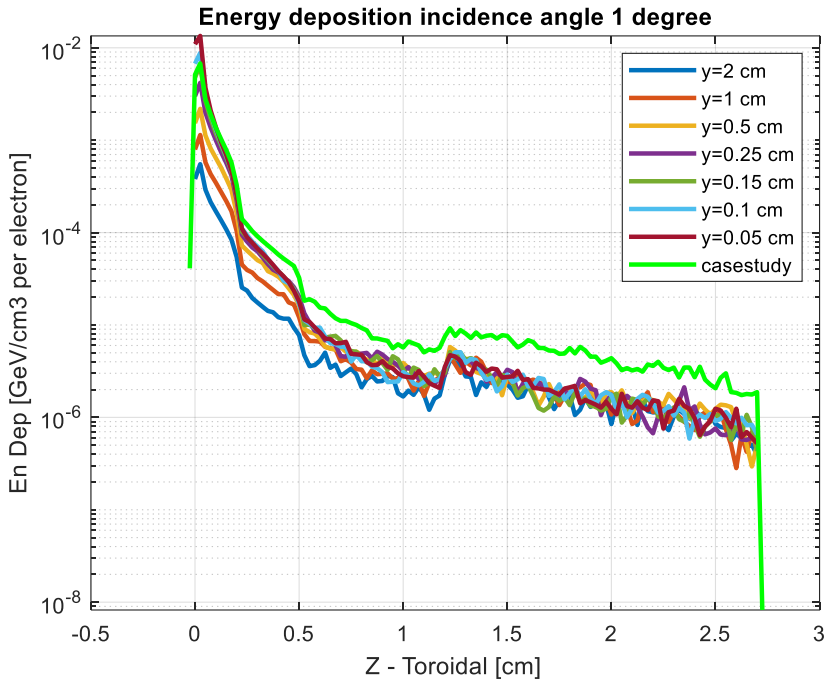

Figure 42 1D projection of the deposited energy with different poloidal extensions of Beam1 and comparison with the curve given by the case study

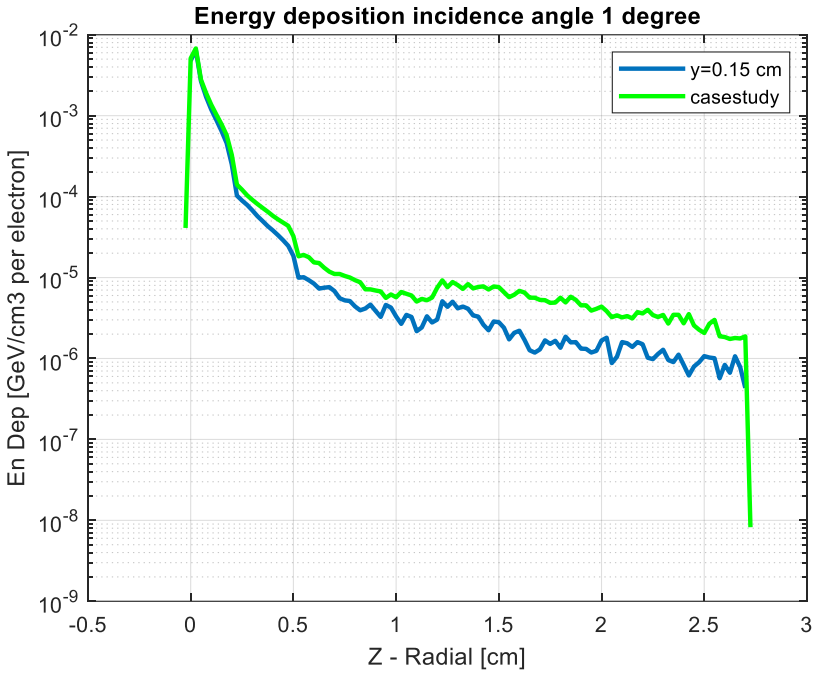

Figure 43 Comparison between the 1D projections of the deposited energy given by the selected Beam1 (blue) and the curve given by the case study (green)

The same behaviour can be observed when the energy deposition curves given by Estimator1 (covering the entire geometry) are compared, as shown in figure 44.

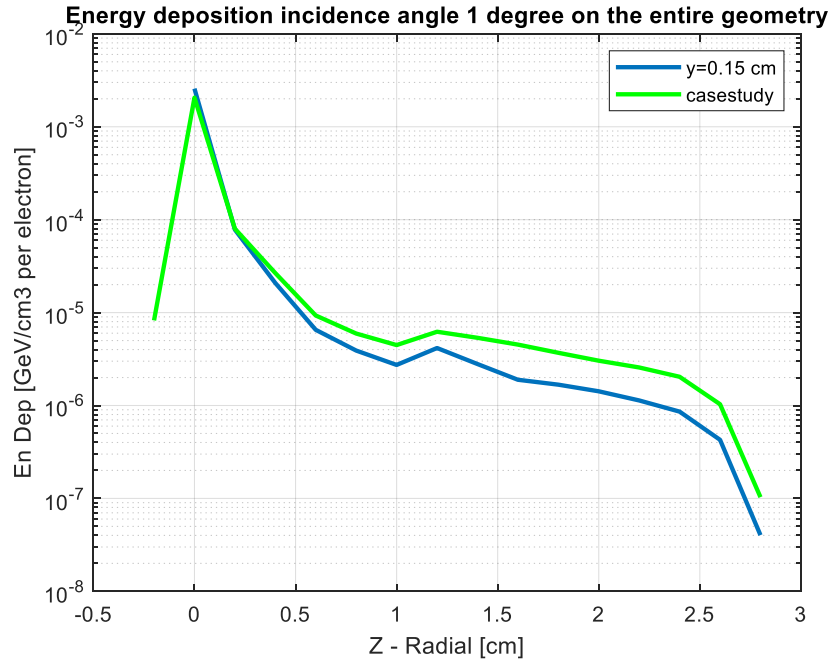

Figure 44 Comparison between the 1D projection of the deposited energies with Beam1 (blue) and case study (green)

In the case of Beam2, however, this difference has not been observed. In figure 45, the energy deposition curves for Beam2 with different poloidal widths are compared with the energy deposition curve of the case study. In particular, y=2 cm, y=1.75 cm, y=1.5 cm, y=1.25 cm and y=1 cm poloidal widths have been used. It can be seen in the figure that as the poloidal extension of the Beam1 reduces, the curve peak at Z=0 cm tends to higher values. However, the influence of this reduction is not as significant as with the results given by Beam1 in figure 43.

In the case of the Beam2, all 5 extensions give curves that are similar to the curve of the case study. However, the beam with y=1.25 cm has been selected as Beam2 based on a quantitative comparison and it can be seen in figure 46 that the two curves are in good agreement.

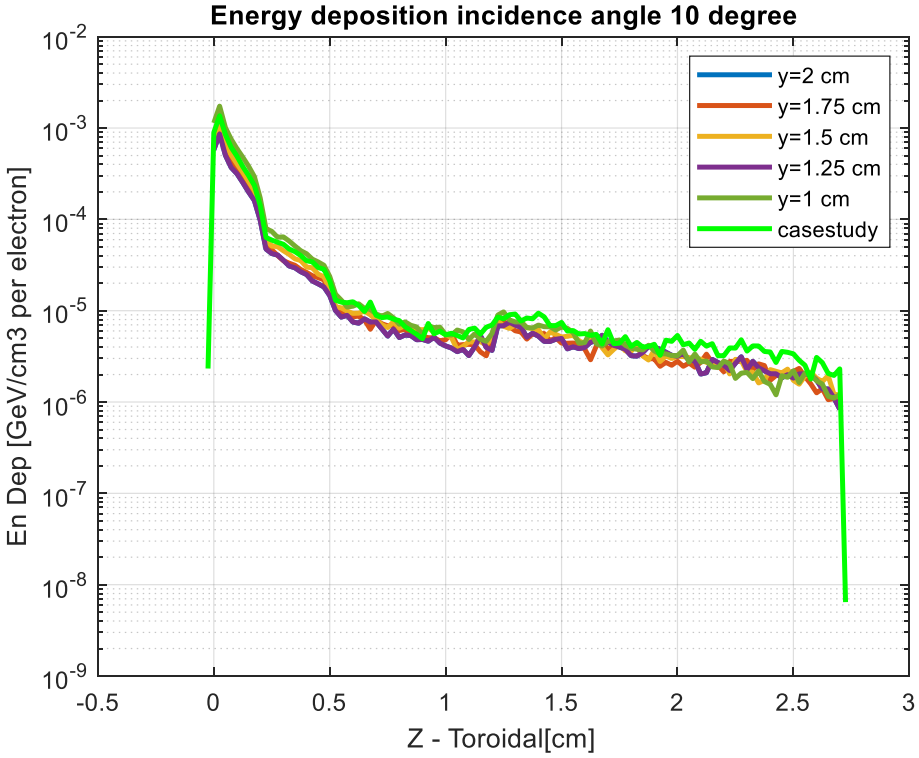

Figure 45 1D projection of the deposited energy with different poloidal extensions of Beam2 and comparison with the curve given by the case study

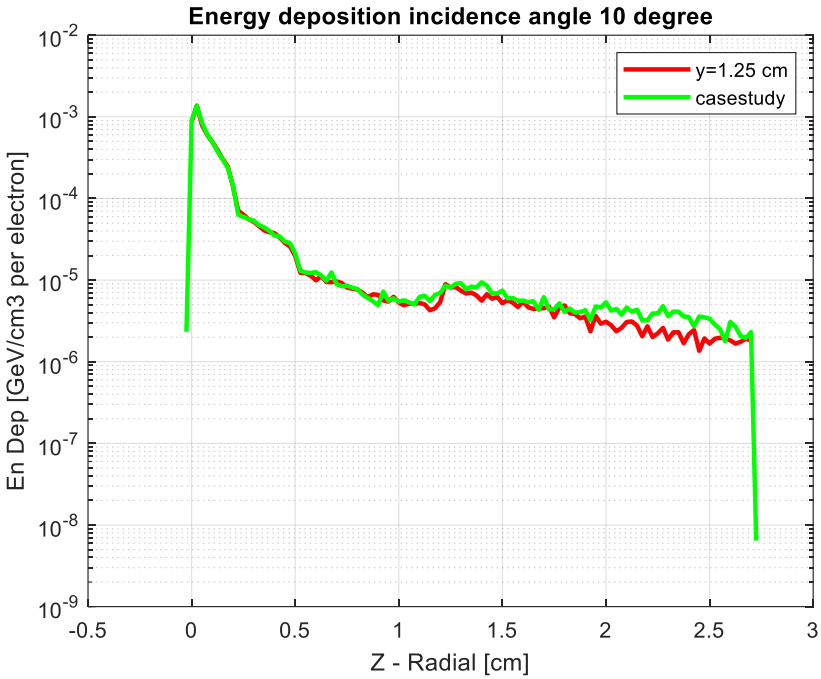

Figure 46 Comparison between the 1D projections of the deposited energy given by the selected Beam2 (blue) and the curve given by the case study (green)

Along with a qualitative comparison, a quantitative comparison about the total deposited energy has been made. In table 5, the total deposited energy estimated by Estimator2 with different Beam1 is reported.

Table 5 Total deposited energy estimated by Estimator2 and different Beam1

Poloidal width [cm]	Deposited energy [MeV per particle]
2	2.34e-2
1	4.59e-2
0.5	8.38e-2
0.25	1.43e-1
0.15	1.99e-1
0.1	2.52e-1
0.05	3.48e-1

The energy deposited estimated by the case study with Beam1 is 2.21e-1 MeV per particle, which is nearest to the energy deposited by Beam1 with poloidal width y=0.15 cm.

For Beam2 table 6 reports the deposited energy estimated by Estimator2 with Beam2 of different poloidal extensions.

Table 6 Total deposited energy estimated by Estimator2 and different Beam2

Poloidal width [cm]	Deposited energy [MeV per particle]
2	4.06e-2
1.75	4.50e-2
1.5	5.25e-2
1.25	6.16e-2
1	7.61e-2

The energy deposited estimated by the case study with Beam2 is 6.29e-2 MeV per particle, which is nearest to the energy deposited by Beam2 with poloidal width y=1.25 cm.

Multiple reasons could explain the difference in the results between the case study and this study:

- Eurofer composition is not defined in the ENEA case study, so an arbitrary Eurofer composition has been assumed in this study that is Eurofer97 RAFM. In order to verify if there is any difference in the results due to a different Eurofer composition, the composition reported in table 7 has been utilized to run a simulation with Beam1 and Beam2 (Zilnyk et al., 2015).
  The results with Beam1 have led to an energy deposition of 1.99e-1 MeV per particle which is equal to the value obtained with the previous composition. On the other hand, for Beam2 the composition reported in table 7 has led to an energy of 6.28e-2 MeV per particle. With respect to 6.29e-2 MeV per particle given by the case study, this is better than 6.16e-2 MeV per particle given by the composition reported in table 1.

Table 7 Eurofer-97 chemical composition (Zilnyk et al., 2015)

Element	%	Element	%
Cr	9.08	C	0.105
W	1.07	N	0.039
Mn	0.56	O	0.0008
V	0.235	Fe	88.7754
Ta	0.125		

- The position of the coolant channels is not the same in the two studies. This can be observed comparing figure 47 taken from the report of the ENEA case study with figure 30. This is because in the original study the position of the channels is not specified, and an arbitrary starting point of the channels has been assumed for this work.

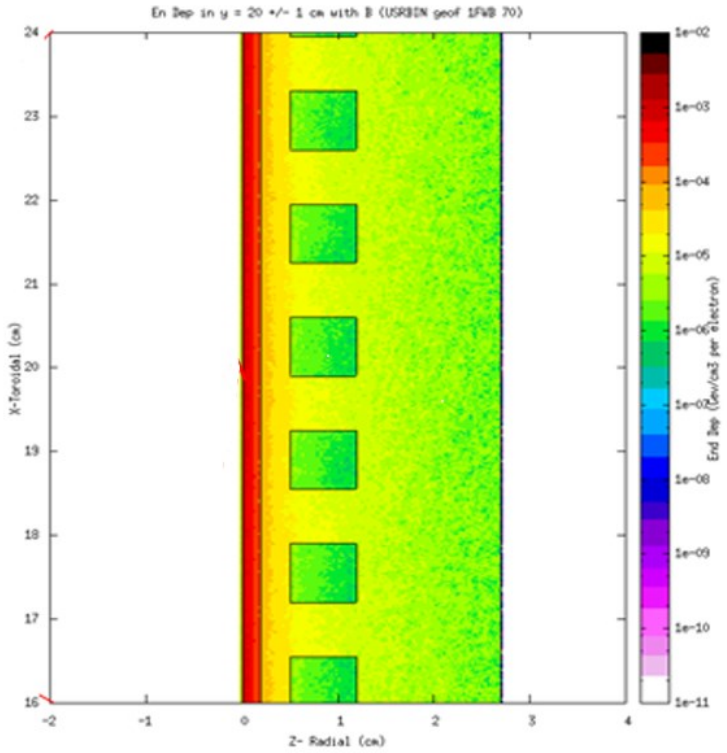

Figure 47 Coolant channels position in the geometry of the ENEA case study (Federici, 2019)

- The estimators used in the two studies are affected by errors that tend to increase with an increasing radial position as shown during the discussion of the results.

8. Runaway Electrons Beams observed in JET

The second part of the study consisted in the reproduction of the REs energy distribution curves obtained in JET. These energy distribution functions are carried out through a reconstruction of the spectral analysis given by the diagnostics present in JET. The diagnostics consist in Hard X-ray (HXR) spectrometers which detect the REs radiation losses through Bremsstrahlung (Dal Molin et al., 2021). This form of radiation is emitted in the Hard X-ray range since the REs can reach energies up to 10 MeV. In figure 48, the HXR spectrometers location in JET is shown.

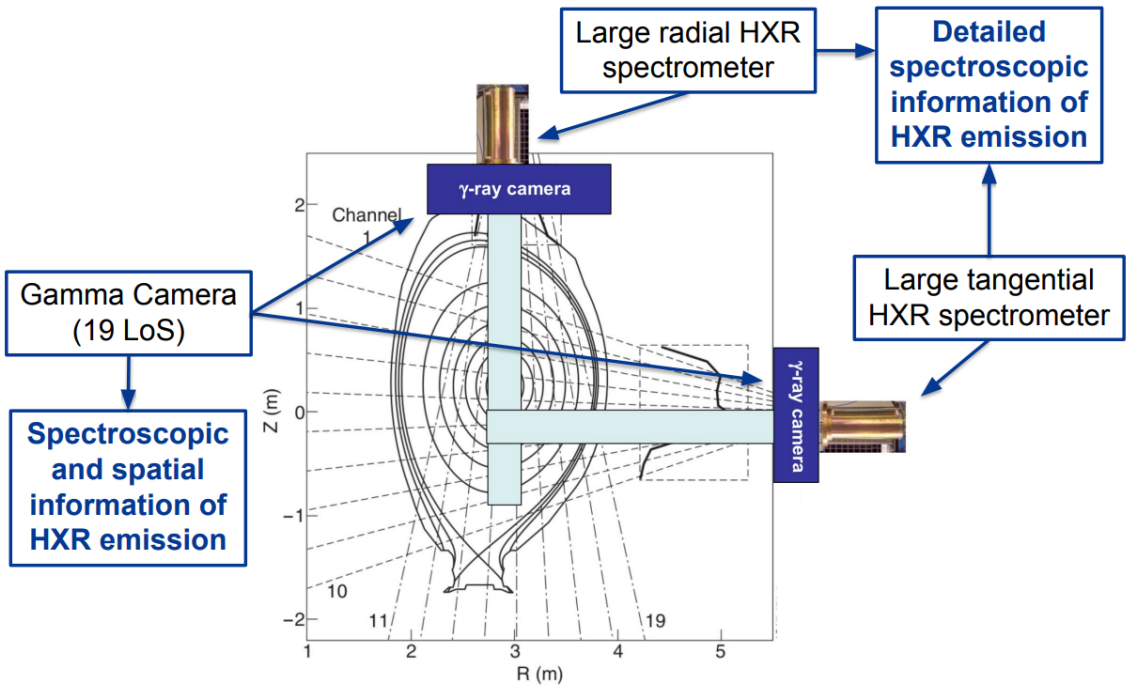

Figure 48 HXR Spectrometers position in JET (Dal Molin et al., 2021)

In figure 48, the radial and tangential spectrometers are reported that give detailed spectroscopic information about the Hard X-ray emissions thanks to a large number of lines of sight (LoS). The line of sight defines the area that is covered by the camera.

The Bremsstrahlung radiation is produced when the runaway electron is decelerated by atomic nuclei present in the matter and the residual energy is emitted in the form of an X-ray. This happens when the REs beam interacts with the limiters present at the wall. In figure 49, some of the scenarios where the REs beam hit the wall are shown. In particular, shots 95135, 95771, and 95776 are

reported since these shots have led to the formation of a runaway beam that ends up at the limiter wall.

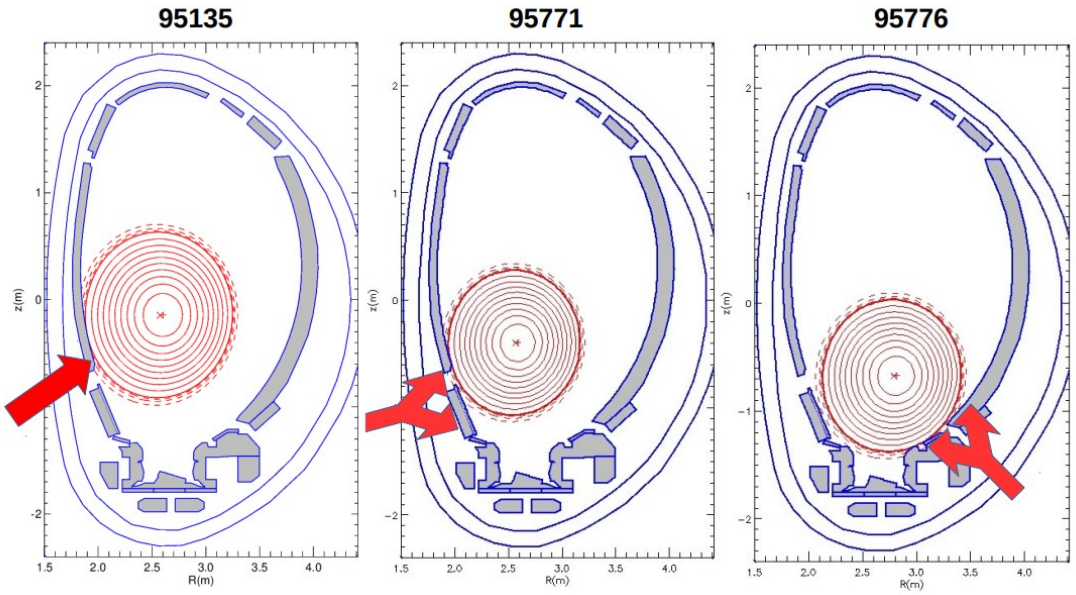

Figure 49 Locations where the REs-limiter interactions take place (Coffey et al., 2021)

The interaction causes the Bremsstrahlung radiation in the HXR range detected by the spectrometers shown in figure 48. The spectrum measured by the diagnostics is shown in figure 50 (left) for shot 95125 which is one of a series of shots where the HXR caused by REs has been measured. Moreover, thanks to a reconstruction technique the energy deposition curve has been obtained (right) (Dal Molin et al., 2021).

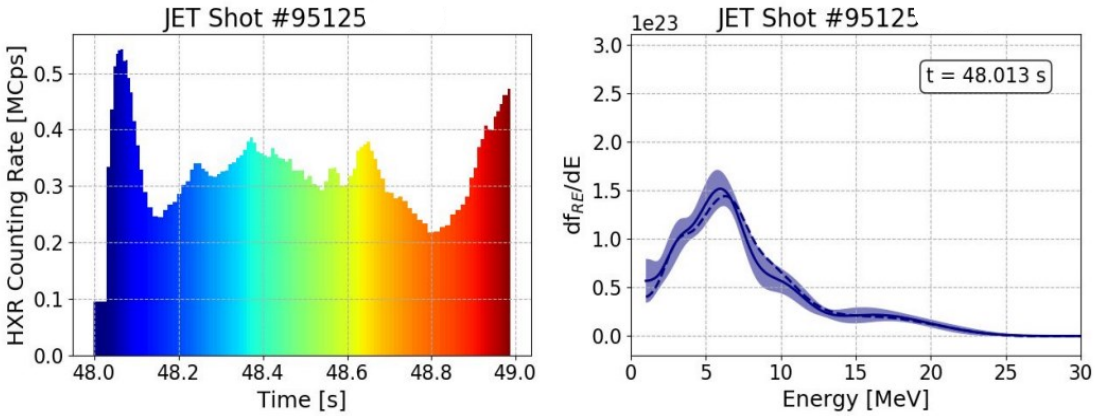

Figure 50 HXR spectrum (left) and the reconstructed energy distribution curve (right) for shot 95125 (Dal Molin et al., 2021)

The second shot that has been considered is the 95131 reported in figure 51. In particular, in the figure, it can be observed that the REs generation has been provoked through Ar injection through MGI and the injection of Ar pellets has led to the formation of a second gaussian in the energy distribution curve. That is some electrons of the REs population has acquired higher energies.

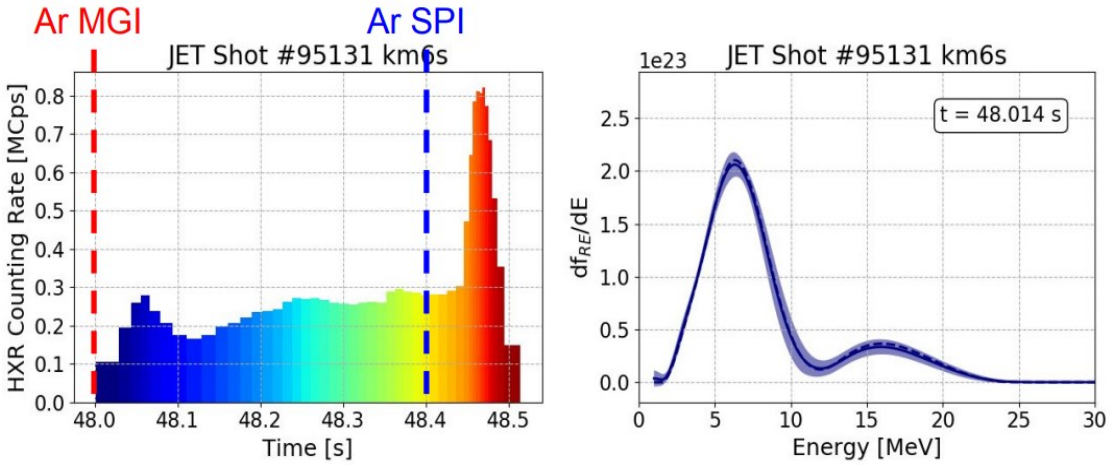

Figure 51 HXR spectrum (left) and the reconstructed energy distribution curve (right) for shot 95131 (Dal Molin et al., 2021)

In this study, the source user routine has been utilized to reproduce the REs energy distribution reported in figures 50 (right) (called Source1 in the following) and 51 (right) (called Source2 in the following). This is because they cannot be implemented in FLUKA using the beam options already available.

The user routine has been used to implement REs with an energy distribution given by a polynomial expression. The latter has been obtained using the cftool of MATLAB which requires in input the coordinates of the points.

Once the polynomial expression is defined it can be written in the user routine to define the particles weight. This is done by defining first the energy interval for the particle energy. From figures 50 (right) and 51 (right), it can be noticed that the energy interval is 0<E<25 MeV. This would define a flat distribution of particles energy, that is, every particle will have the same weight. For instance, the number of particles at 5 MeV would be equal to the number of particles at 10 MeV. This was the case of the REs beam considered in the EU-DEMO FW analysis.

In order to reproduce a gaussian energy distribution, a function called *particle_weight* in the user routine has to be used. In this work, the particle weight is approximated through a polynomial expression. For instance, if figure 51 (right) is considered, the number of particles simulated with an energy of 6 MeV

would be 5 times $(^2/_{0.4})$ higher than the number of particles with an energy of 16 MeV.

Once the user routine is ready it is compiled in the FLAIR environment and the simulation is run with the estimator USRBDX.

The curves obtained in MATLAB are shown in figures 52 and 53 along with the polynomial expressions given by the tool. The curves are in good agreement with the points as is shown by the values of R-square being equal to 0.9964 for Source1 and 0.9999 for Source2.

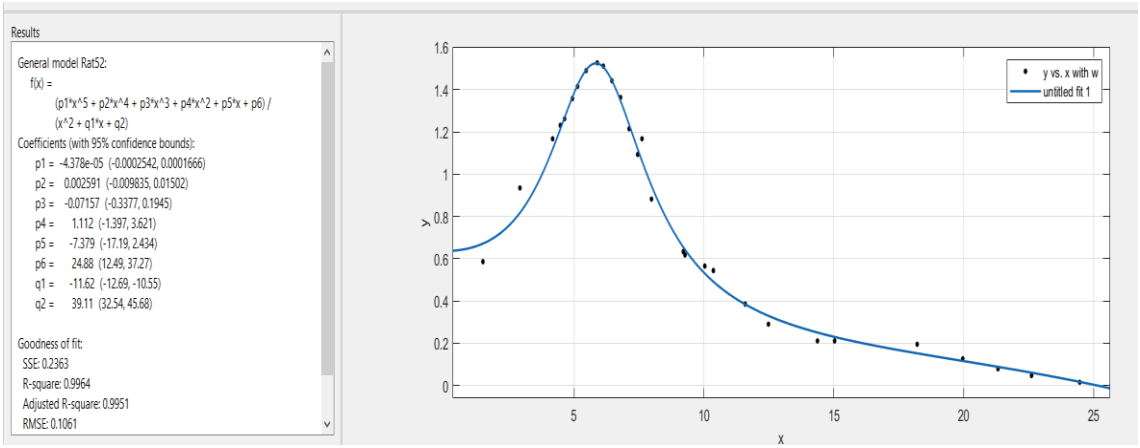

Figure 52 Source1 curve obtained through cftool and the relative polynomial expression

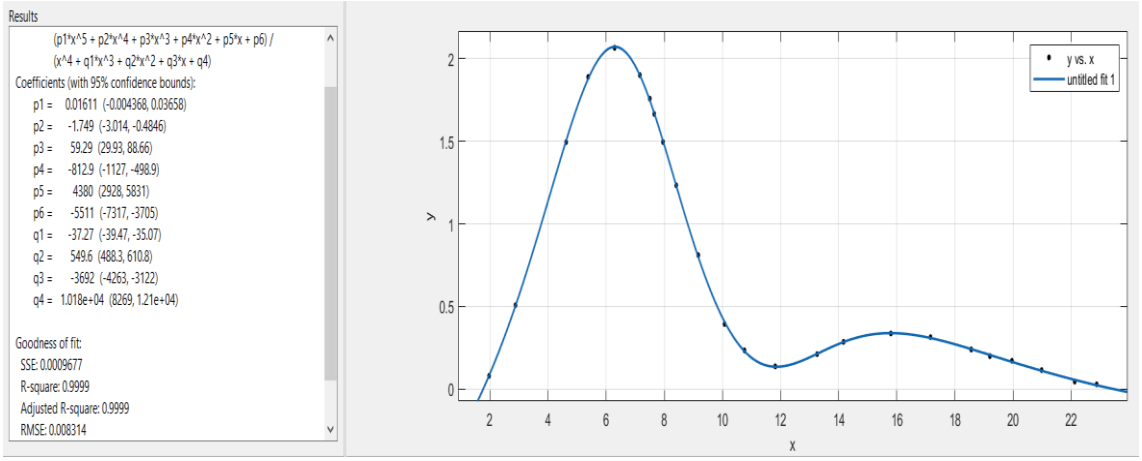

Figure 53 Source1 curve obtained through cftool and the relative polynomial expression

The x-axis of figures 52 and 53 represents the energy in MeV and the y-axis is the weight of the particles. Once the polynomial expressions are obtained, they are written in the user routine file and the files are compiled in FLAIR. The results

with the relative error bars given by the estimator are shown in figures 54 and 55.

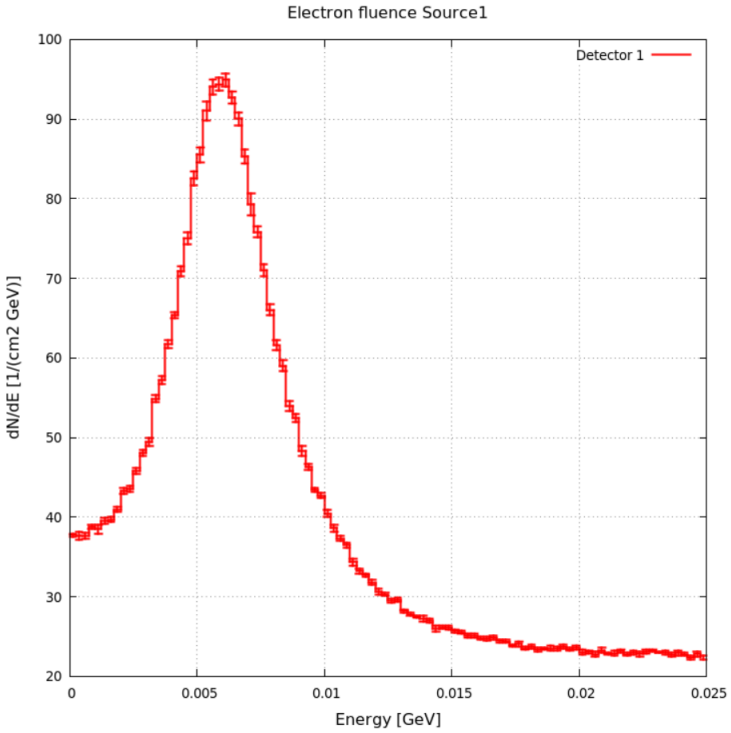

Figure 54 REs fluence estimated by USRBDX for Source1

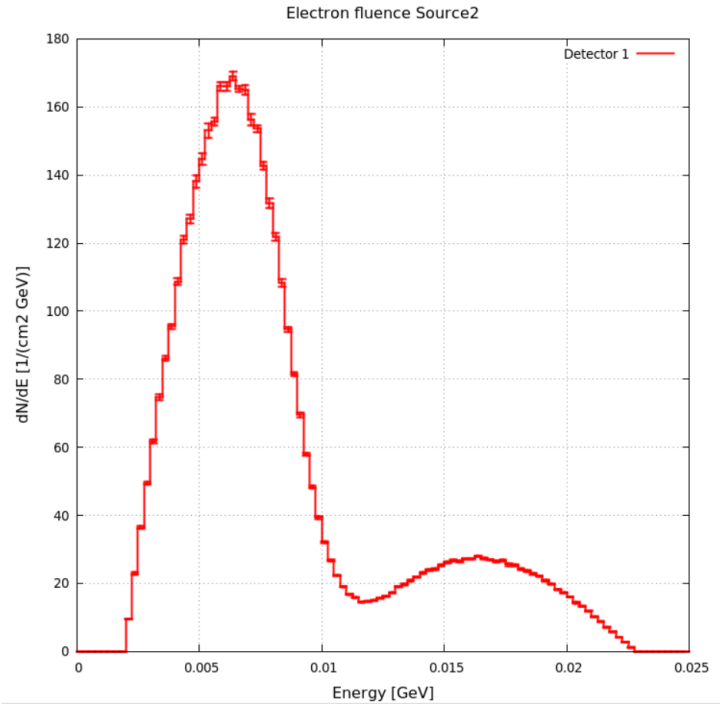

Figure 55 REs fluence estimated by USRBDX for Source2

The results are obtained with a number of 1e6 particles divided into 10 cycles in order to obtain an accurate output. The electron fluence given by FLUKA approximates very well the reconstructed energy distributions obtained from the HXR Spectrometry.

In order to estimate the energy deposition curve in the limiter which is made in Beryllium (Be), a simple sample in Be was considered. The sample dimensions are 0<X<30, 19<Y<21, and 0<Z<2.7, and the REs beam hit the sample at X= 15 cm, Y= 20 cm and Z=0 cm with an incidence angle of 10 degrees. A 3D representation of the geometry is given in figure 56 along with the beam direction (purple).

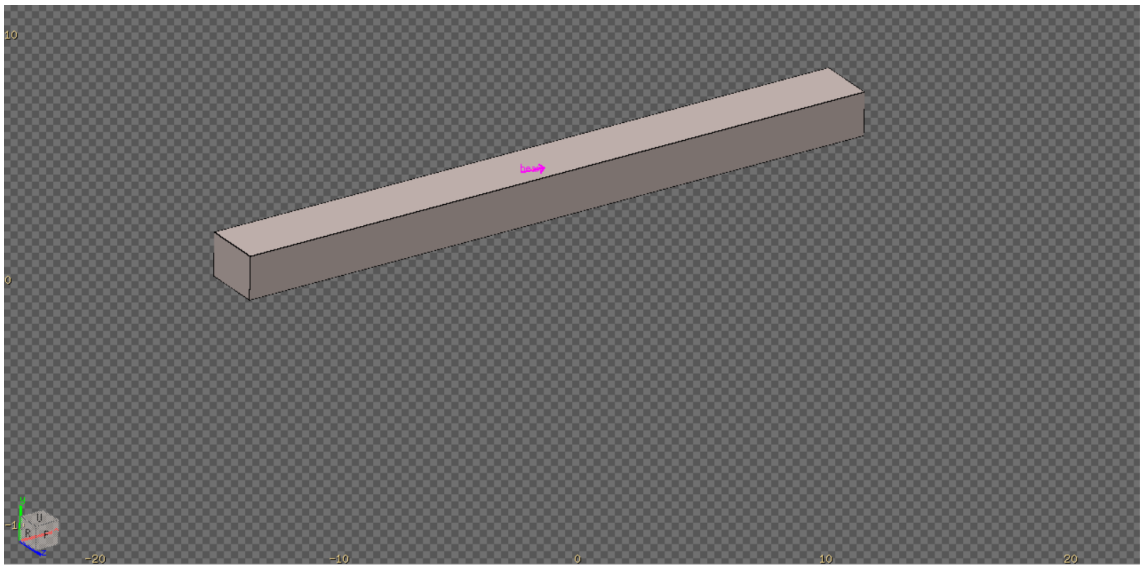

Figure 56 3D representation of the Be sample and the beam direction (purple)

In figure 57, the results of the simulation with Source1 (blue) and Source2 (red) are compared. It can be observed that Source1 leads to a lower deposition with respect to Source2. The reason for this behavior is related to the fact that Source2 is constituted by several particles that have higher energy with respect to the Source1 particles.

The simulation has been done with a basic sample to observe the behavior of Berylium under irradiation, however, in the future, this work would be useful to study the impact of these sources on the JET wall using FLUKA. In addition, since it has been shown that FLUKA can reproduce the experimentally observed REs energy distributions, more complicated sources observed in other reactors can also be built and their impact on the FW geometry simulated.

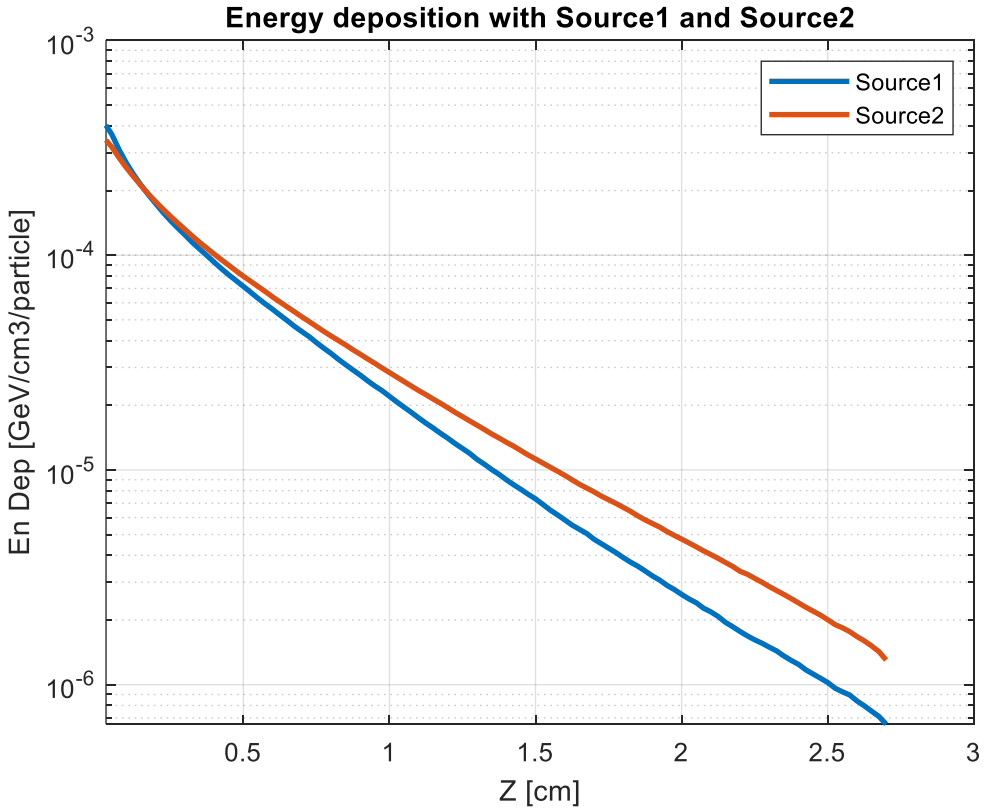

Figure 57 Comparison between the 1D projection of the deposited energy with Source1 and Source2

9. Conclusion and Perspectives

This thesis focuses on the study of runaway electrons and their impact on the FW of different fusion reactors. Firstly, an introduction to the basic concepts of a tokamak machine is given to get familiar with different terms used during the analysis of runaway electron physics. In this framework, a description of the problems caused by the REs in the past is given. Indeed, it has been seen that the REs have damaged the structure of many of the existing reactors including JET, TORE SUPRA, Doublet III, etc. Moreover, the simulations of the REs impact on the structure of the future reactors would exponentially increase the threat represented by these electrons.

Due to damage that they can cause to the reactors, the study of their generation mechanisms is under great focus. It has been demonstrated that while in the current reactor the Dreicer mechanism represents the primary mechanism of REs generation in the future reactors the role will be taken up by the avalanche mechanism. The Dreicer mechanism takes place when during the current quench phase of a disruption, the toroidal electric field overcomes the critical electric field leading to a continuous acceleration of the electrons that reach relativistic speed. The avalanche mechanism, instead, is related to the e-fold increase in the REs population. Since at higher energies the drag force acting on the electrons decreases rapidly and the collision events reduce drastically, the electrons travel larger distances and the presence of the toroidal electric field leads to their acceleration. Along their path, they can encounter atoms causing the generation of secondary electrons that accelerate to higher energies continuing the avalanche process. Simulation done on ITER has shown that the avalanche mechanism would be responsible for an e-fold growth equal to 50. This strengthens the need for suppression and mitigation systems.

Currently, there are four suppression and mitigation system consisting in injecting impurities in plasma or exploiting the magnetic fields present in it to increase its radiation losses. The MGI, however, can cause an additional generation of REs if only argon is used as an impurity gas and for this reason, a mixture of deuterium and argon is mainly used in the current reactors. On the other hand, the SPI system causes a rapid reduction in the electron temperature which translates into a higher resistive electric field in the plasma, this electric field may overcome the critical field and leads to runaway generation. The RMP system consists in using external coils to suppress or mitigate the runaway electrons by enhancing their radial losses by inducing magnetic perturbation in the plasma, however, due to the larger size of the future tokamaks, there would be a larger distance between the RMP coils and the plasma core leading to additional problems in suppressing the runaway electrons. The MET system aims at reducing the toroidal electric field which is developed during the current

quench phase by transferring the plasma poloidal magnetic energy out of the vacuum vessel through the use of energy transfer coils, nevertheless, its use has been demonstrated only in J-TEXT and further investigation is necessary to take it in consideration for the design of larger reactors.

The second part of this paper has focused on the practical work done in the framework of this thesis. The Monte Carlo code FLUKA has been used to carry out this work due to the multiple advantages offered by the code environment. Indeed, it can simulate the transport of about 60 different particle species in a wide range of energy. It is paired with a user-friendly interface FLIAR based on python language with C++ extension used for the geometry visualization. Thanks to this feature it is possible to design the geometry interactively by visualizing the designed geometry in real-time.

FLUKA contains multiple estimators able to trace the energy deposition and particle fluence in the material. These estimators are affected by statistical and systematic uncertainties. The statistical uncertainties can be reduced by simulating a large number of test particles since the error goes down as $1/\sqrt{n}$ where n is the total number of particles. The systematic uncertainties depend on the used models and beam losses that are not simple to evaluate or to reduce.

Apart from the built-in sources and estimators, FLUKA contains also some user routines that can be extracted through the FLAIR environment. The extracted routines can be modified to define specific sources or estimators and then compiled again in FLUKA.

For the first part of the practical work regarding the REs impact on EU-DEMO FW, no additional user routines have been used while for the reproduction of the REs energy distributions observes in some of the JET shots a source routine has been utilized.

The first part consisted in irradiating a sample geometry of the EU-DEMO FW with 20 MeV REs beam with an incidence angle of 1 degree (called Beam1) and 10 degrees (called Beam2). The results have shown that the deposited energy differs with the incidence angle. In particular, a beam hitting with 10 degrees incidence angle leads to a higher energy deposition with respect to a beam hitting with 1 degree incidence angle. The total deposited energy with Beam1 is around 6.4 MeV and 10.54 MeV with Beam2. The tungsten layer takes up around 85% of the total deposited energy with Beam1 and 74% with Beam2. This is because with an incidence angle of 1 degree the electrons have to travel a distance that is 10 times greater than the distance travelled by the electrons with an incidence angle of 10 degrees to reach a certain radial depth. This increases also the probability that the electrons escape from the system leading to a lower total energy deposition with Beam1. The high stopping power of tungsten demonstrates its capability to protect the structural material behind it.

The deposited energy in the whole geometry is not affected by the poloidal extension of a Beam as it has been seen with Beam1. However, if a fraction of the total geometry is considered, the poloidal width of the beam plays a significant role. Since Beam1 has a poloidal width of 0.15 cm, a higher amount of energy is traced by the Estimator2 which has a poloidal width of 0.05 cm, whereas Beam2 with 1.25 cm of poloidal width distributes its energy on a larger surface and only a small fraction of it is detected by the estimator.

Since the poloidal length of the beams is not given in the report of the ENEA case study, a comparison has been made between the results of this work and the original case study, and it was found that Beam1 may have a poloidal width of 0.15 cm while Beam2 a poloidal width of 1.25 cm. There are still differences between the results, and these could be explained by a possible different Eurofer composition, different coolant channels position, and the errors of the estimators.

The last part of the work consisted in reproducing the REs energy distributions observed in JET. These distributions (called Source1 and Source2) have been reconstructed from the HXR spectrometer diagnostics present in the JET machine. These X-rays are the secondary particles generated by the REs and could be traced by the virtual detectors embedded in FLUKA. It has been shown that the code can reproduce these REs with good accuracy. Furthermore, REs irradiation of a Beryllium sample has been carried out to observe that Source1 which consists of a single gaussian leads to a lower energy deposition with respect to Source2. This is because Source2 consists of a double gaussian with the particles represented by the second gaussian being at higher energy values with respect to the particles of Source1.

In the future, this work would be useful to reproduce, to a certain extent, the impact of the REs on the JET FW structural materials. Therefore, this would show the capabilities of FLUKA in reproducing the real measurements, clearing the picture of how REs interacts with the different structural materials present in the main chamber of JET. Afterward, the study could be scaled up to EU-DEMO where Tungsten will be the main plasma-facing component to handle the REs.

Finally, in this study, a simple geometry has been implemented to study the impact of REs on EU-DEMO FW, but FLUKA allows to implement more complex geometries through external tools. This tool will be used in the future to study the behavior of complex geometries under REs irradiation.

Bibliography

Bakhtiari, M., Kawano, Y., Tamai, H., Miura, Y., Yoshino, R., & Nishida, Y. (2002). Fast plasma shutdown scenarios in the JT-60U tokamak using intense mixed gas puffing. Nuclear fusion, 42(10), 1197.

Ballarini, F., Battistoni, G., Campanella, M., Carboni, M., Cerutti, F., Empl, A., ... & Vlachoudis, V. (2006, May). The FLUKA code: an overview. In Journal of Physics: Conference Series (Vol. 41, No. 1, p. 014). IOP Publishing.

Bartels, H. W. (1994). Impact of runaway electrons. Fusion engineering and design, 23(4), 323-328.

Barton, J. E., Wehner, W. P., Schuster, E., Felici, F., & Sauter, O. (2015, July). Simultaneous closed-loop control of the current profile and the electron temperature profile in the TCV tokamak. In *2015 American Control Conference (ACC)* (pp. 3316-3321). IEEE.

Bolt, H., Miyahara, A., Miyake, M., & Yamamoto, T. (1987). Simulation of tokamak runaway-electron events. Journal of Nuclear Materials, 151(1), 48-54.

Bozhenkov, S. A., Lehnen, M., Finken, K. H., Jakubowski, M. W., Wolf, R. C., Jaspers, R., ... & TEXTOR team. (2008). Generation and suppression of runaway electrons in disruption mitigation experiments in TEXTOR. Plasma physics and controlled fusion, 50(10), 105007.

Cai, N., Zhang, M., Yang, Y., Chen, Z., Zhang, J., Rao, B., ... & J-TEXT Team. (2021). Suppression of runaway current by magnetic energy transfer in J-TEXT. Fusion Engineering and Design, 169, 112488.

Chen, Z. Y., Chen, Z. P., Zhang, Y., Jin, W., Fang, D., Ba, W. G., ... & J-TEXT Team. (2012). Study of the generation and suppression of runaway currents in provoked disruptions in J-TEXT. Physics Letters A, 376(24-25), 1937-1941.

Cizek, J., Vilemova, M., Lukac, F., Koller, M., Kondas, J., & Singh, R. (2019). Cold sprayed tungsten armor for tokamak first wall. *Coatings*, *9*(12), 836.

Coffey, I., Pautasso, G., Reux, C., Sertoli, M., & Silburn, S. (2021, March 2021), T17-13: Reconstruction of the runaway electron energy distribution function by spectral analysis of the HXR emission at JET, [PowerPoint Presentation].

Dal Molin, A., Gorin, G., Panontin, E., & Nocente, M. (n.d.), T17-13: Reconstruction of the runaway electron energy distribution function by spectral analysis of the HXR emission at JET, [PowerPoint Presentation].

De Vries, P. C., & Gribov, Y. (2019). ITER breakdown and plasma initiation revisited. *Nuclear Fusion*, *59*(9), 096043.

Ding, N., Huang, L., & Qiu, X. M. (1999). Alfven wave current drive in tokamak rotating plasma with negative magnetic shear. *Physics of Plasmas*, *6*(12), 4633-4644.

Dubus, G. D. (2014). From plain visualisation to vibration sensing: using a camera to control the flexibilities in the ITER remote handling equipment.

Fasoli, A. (2010). Kinetic theory of plasmas. Plasma Physics II, Ecole Polytechnique Federale de Lausanne.

Federici, G., Use of the FLUKA code for the evaluation of volumetric loads due to Res (runaway electrons).

Ferrari, A., Sala, P. R., Guaraldi, R., & Padoani, F. (1992). An improved multiple scattering model for charged particle transport. *Nuclear Instruments and Methods in Physics Research Section B: Beam Interactions with Materials and Atoms*, *71*(4), 412-426.

FLUKA, (2020), Introduction to the Monte Carlo simulation of radiation transport [Powerpoint Presentation]. Beginner online training, Fall 2020.

FLUKA, (2020), Scoring physics quantities [Powerpoint Presentation]. Beginner online training, Fall 2020.

Freidberg, J. P. (2008). *Plasma physics and fusion energy*. Cambridge university press.

Fulop, T., Papp, G., Pokol, G., Komar, A., Feher, T., Stahl, A., Landreman, M. (2013, October 16), Kinetic instabilities driven by runaway electrons, [PowerPoint Presentation]. Chamles University of Technology.

Gill, R. D., Alper, B., De Baar, M., Hender, T. C., Johnson, M. F., & Riccardo, V. (2002). Behaviour of disruption generated runaways in JET. *Nuclear fusion*, *42*(8), 1039.

Group, T. (1980). Activation effects due to runaway beams on TFR. Journal of Nuclear Materials, 93, 203-209.

Jarvis, O. N., Sadler, G., & Thompson, J. L. (1988). Photoneutron production accompanying plasma disruptions in JET. Nuclear fusion, 28(11), 1981.

Jayakumar, R., Fleischmann, H. H., & Zweben, S. J. (1993). Collisional avalanche exponentiation of runaway electrons in electrified plasmas. *Physics Letters A*, *172*(6), 447-451.

Kawamura, T., Obayashi, H., & Miyahara, A. (1989). On the generation of runaway electrons and their impact to plasma facing components. Fusion Engineering and Design, 9, 39-44.

Kemaneci, E. H. (2009). Numerical investigation of a dc glow discharge in an argon gas: two-component plasma model (Master's thesis, Middle East Technical University).

Lehnen, M., Abdullaev, S. S., Arnoux, G., Bozhenkov, S. A., Jakubowski, M. W., Jaspers, R., ... & Textor Team. (2009). Runaway generation during disruptions in JET and TEXTOR. Journal of nuclear materials, 390, 740-746.

Lehnen, M., Bozhenkov, S. A., Abdullaev, S. S., Jakubowski, M. W., & TEXTOR team. (2008). Suppression of runaway electrons by resonant magnetic perturbations in TEXTOR disruptions. Physical review letters, 100(25), 255003.

Maddaluno, G., Maruccia, G., Merola, M., & Rollet, S. (2003). Energy deposition and thermal effects of runaway electrons in ITER-FEAT plasma facing components. Journal of nuclear materials, 313, 651-656.

Nishikawa, M., Team, J., Yokomizo, H., Kitsunezaki, A., Mckelvey, T. E., Taylor, T. S., ... & Seraydarian, R. (1984). Graphite limiter damage due to runaway electrons and abrupt Ip termination in doublet III. Journal of Nuclear Materials, 128, 493-499.

Nordlund, K. H. (2018). European Research Roadmap to the Realisation of Fusion Energy.

Nygren, R., Lutz, T., Walsh, D., Martin, G., Chatelier, M., Loarer, T., & Guilhem, D. (1997). Runaway electron damage to the Tore Supra Phase III outboard pump limiter. Journal of nuclear materials, 241, 522-527.

Paúl, A., Beirante, A., Franco, N., Alves, E., & Odriozola, J. A. (2006). Phase transformation and structural studies of EUROFER RAFM alloy. In *Materials science forum* (Vol. 514, pp. 500-504). Trans Tech Publications Ltd.

Plyusnin, V. V., Pereira, R., Fernandes, A., Kiptily, V., Arnoux, G., Hender, T., ... & De Vries, P. (2012). Latest progress in studies of runaway electrons in JET.

Reux, C., Plyusnin, V., Alper, B., Alves, D., Bazylev, B., Belonohy, E., ... & Sozzi, C. (2015). Corrigendum: Runaway electron beam generation and mitigation during disruptions at JET-ILW (2015 Nucl. Fusion 55 093013). Nuclear Fusion, 55(12), 129501.

Rosenbluth, M. N., & Putvinski, S. V. (1997). Theory for avalanche of runaway electrons in tokamaks. Nuclear fusion, 37(10), 1355.

Russo, A. J., & Campbell, R. B. (1993). A model for disruption generated runaway electrons. Nuclear fusion, 33(9), 1305.

Siccinio, M. (2019, January 8), Disruptions – towards ITER and DEMO, [PowerPoint Presentation]. Politecnico di Torino, Torino, Italia.

Sizyuk, V., & Hassanein, A. (2009). Self-consistent analysis of the effect of runaway electrons on plasma facing components in ITER. Nuclear Fusion, 49(9), 095003.

Zilnyk, K. D., Oliveira, V. B., Sandim, H. R. Z., Möslang, A., & Raabe, D. (2015). Martensitic transformation in Eurofer-97 and ODS-Eurofer steels: A comparative study. *Journal of Nuclear Materials*, *462*, 360-367.